Received: 12 August 2020 | Revised: 9 October 2020 | Accepted: 2 November 2020

DOI: 10.1111/jace.17582

ORIGINAL ARTICLE

Journal of the American Ceramic Society

Synthesis, sintering, and effect of surface roughness on oxidation of submicron Ti_2AlC ceramics

Sylvain Badie[1,2] | **Apurv Dash**[1,2] | **Yoo Jung Sohn**[1] | **Robert Vaßen**[1] | **Olivier Guillon**[1,2,3] | **Jesus Gonzalez-Julian**[1,2]

[1]Institute of Energy and Climate Research: Materials Synthesis and Processing (IEK-1), Forschungszentrum Jülich GmbH, Jülich, Germany

[2]Department of Ceramics and Refractory Materials, Institute of Mineral Engineering, RWTH Aachen University, Aachen, Germany

[3]Jülich Aachen Research Alliance, JARA-Energy, Jülich, Germany

***Correspondence**
Sylvain Badie, Forschungszentrum Jülich GmbH, Institute of Energy and Climate Research: Materials Synthesis and Processing (IEK-1), 52425 Jülich, Germany.
Email: s.badie@fz-juelich.de

Funding information
Ministry of Education, Grant/Award Number: 03SF0534; Bundesministerium für Bildung und Forschung, Grant/Award Number: 03SF0534; EDS

Abstract

Submicron Ti_2AlC MAX phase powder was synthesized by molten salt shielded synthesis (MS^3) using a Ti:Al:C molar ratio of 2:1:0.9 at a process temperature of 1000°C for 5 hours. The synthesized powder presented a mean particle size of ~0.9 μm and a purity of 91 wt. % Ti_2AlC, containing 6 wt. % Ti_3AlC_2. The Ti_2AlC powder was sintered by pressureless sintering, achieving a maximal relative density of 90%, hence field-assisted sintering technology/spark plasma sintering was used to enhance densification. The fine-grained microstructure was preserved, and phase purity of Ti_2AlC was unaltered in the latter case, with a relative density of 98.5%. Oxidation was performed at 1200°C for 50 hours in static air of dense monolithic Ti_2AlC with different surface finish, (polished, ground and sandblasted) which resulted in the formation of an approx. 8 μm thin aluminum oxide (Al_2O_3) layer decorated with titanium dioxide (rutile, TiO_2) colonies. Surface quality had no influence on Al_2O_3 scale thickness, but the amount and size of TiO_2 crystals increased with surface roughness. A phenomenon of rumpling of the thermally grown oxide (TGO) was observed and a model to estimate the extent of deformation is proposed.

KEYWORDS

FAST/SPS, MAX phases, molten salt shielded synthesis, oxidation behavior, Ti_2AlC

1 | INTRODUCTION

The ternary carbides and nitrides of general formula $M_{n+1}AX_n$, where M corresponds to an early transition metal, A to an A-group element (mainly IIIA and IVA) of the periodic table and X being either carbon or nitrogen, have received considerable attention in the past two decades.[1] These nanolaminated structures possess an unusual combination of both ceramic and metallic features. In addition to good thermal and electrical conductivities, this unique nature endows them with good elastic stiffness, machinability, high fracture toughness, thermal shock resistance, and damage tolerance.[1,2] In addition, Al-containing MAX phases exhibit excellent oxidation resistance and a self-healing ability.[3,4] Being encompassed in the category of alumina-forming materials, their outstanding oxidation resistance emanates from the formation of a protective slow growing Al_2O_3 scale. Especially, Ti_2AlC (8.2×10^{-6}/K between 25°C and 1300°C)[5] arouse interest because of the good match of coefficient of thermal expansion (CTE) to that of Al_2O_3 (8.0×10^{-6}/K and 9.0×10^{-6}/K in the 25°C-1000°C and 25°C-1500°C ranges, respectively),[6] hence reducing thermal stresses at high temperature.

However, synthesis of Ti_2AlC—and in general of all the MAX phase compositions—remains challenging when it comes to finding a compromise between high purity, large quantities (>1 kg) and affordable costs. Ti_2AlC can be synthesized by solid-state reaction methods at high temperature, but the bulk samples must be ground and milled to produce fine powders. First, the milling step consumes time and energy, with the risk of potential contamination and alteration of properties. Second, inert atmospheres are always employed to avoid oxidation of raw materials during synthesis, increasing the costs and complexity of the process. Additionally, the eventuality of upscaling the synthesis process should be considered. Furthermore, the synthesis of MAX phases in the Ti-Al-C system is

TABLE 1 Various reported synthesis routes and corresponding phase composition

Year	Reference	Synthesis route	Raw materials and synthesis parameters	Quantitative phase analysis	Observed phases (mass fraction)
2000	[5]	Reactive hot isostatic pressing	Ti, Al_4C_3, graphite powders, argon, 30 h at 1300°C, 40 MPa	SEM + image analysis	Ti_2AlC (96%), Ti_3P + Al_2O_3 (4%)[a]
2007	[8]	Solid-liquid reaction synthesis	Ti, Al, graphite powders	XRD + Rietveld refinement	Ti_2AlC (>99%)
2016	[11]	Pressureless sintering	Ti, Al, TiC powders with (Ti:Al:TiC = 1.00:1.05:0.95), argon, 1400°C	XRD + SEM +EBSD + image analysis	Ti_2AlC (95.14%), Al_2O_3 (3.3%), TiAl (1.4%), TiC (0.16%)[a]
2010	[12]	Pressureless sintering	Maxthal 211, argon, 1 h at 1500°C	XRD	Ti_2AlC (92%), TiC (5%), Al_2O_3 (3%)[a]
2010	[13]	Spark plasma sintering	CVD in-situ grown CNTs on TiAl particles using $Co(NO_3).6H_2O$ as catalyst, vacuum, 1200°C, 50 kN	XRD	Ti_2AlC (92%), TiC (5%), Ti_2Al_5 (3%)
2015	[14]	(A) Arc melting + (B) annealing + (C) quenching	(A) Ti, Al, graphite powders, argon, 5 min + (B) 6 h at 1350°C + 12 h at 1250°C + 750 h at 650°C + (C) 200°C/s in water	XRD + Rietveld refinement	Ti_2AlC (47%), Ti_3AlC_2 (30%), $TiAl_3$ (23%)
2009	[15]	Self-propagating high-temperature synthesis (SHS)	Ti, Al, carbon black powders + additions of TiC or Al_4C_3 with (Ti:Al:C = 2:1:1), argon	XRD + Peak intensity integration formula	Ti_2AlC (80%–90%), TiC (20%–10%)
2010	[16]	Mechanically activated SHS	Ti, Al, graphite powders, ~2000 K, argon	XRD + Pattern deconvolution	Ti_2AlC (95%), TiC (5%) or (Ti_2AlC + Ti_3AlC_2) (99.7%) when increasing Al content
2019	[17]	SHS	Ti, Al, graphite powders, argon	XRD + Rietveld refinement	Ti_2AlC (95.4%), $TiAl_2$ (4.6%) Ti_2AlC (87.5%), Ti_3AlC_2 (10.8%), TiC (1.6%)
2011	[20]	Proprietary method developed by 3-ONE-2	N/A	XRD + Rietveld refinement	Ti_2AlC (67%), TiC (19%), Ti_3AlC_2 (14%)[b]
2011	[21]	Proprietary method developed by Kanthal AB (Sandvik)	Maxthal 211	XRD + Rietveld refinement	Ti_2AlC (84.3%), Ti_3AlC_2 (6.5%), TiC (5.1%), TiAl (4.1%)
2017	[22]	Proprietary method developed by Kanthal AB (Sandvik), combustion synthesis	Maxthal 211	XRD + Rietveld refinement	Ti_2AlC (68.33%), Ti_3AlC_2 (14.02%), TiC (7.86%), $Ti_{1.2}Al_{0.8}$ (9.79%)
2018	[19]	Molten salt synthesis	Ti, Al, graphite powders, in 50:50 NaCl:KCl mixture, argon, 2 h at 1000°C	XRD + Rietveld refinement	Ti_2AlC (88%), $Ti_{0.9}Al_{1.1}$ (12%)

[a]Volume fraction.

[b]Molar fraction.

usually known for competitive reaction pathways between Ti_2AlC and Ti_3AlC_2 phases, thus restricting purity criteria. Different synthesis routes with diverse outcomes were pursued and some of them (with purity values) are listed in Table 1. Solid-state-based synthesis routes such as reactive hot pressing,[7] reactive hot isostatic pressing,[5] solid-liquid reaction synthesis,[8,9] reactive sintering,[10] pressureless sintering,[11,12] spark plasma sintering,[13] arc melting,[14] and self-propagating high-temperature synthesis (SHS)[15-18] can be distinguished from ionic-liquid medium-assisted routes such as molten salt synthesis.[19]

Barsoum et al.[7] aimed the production of bulk polycrystalline Ti_2AlC via reactive hot pressing (HP) of a $Ti:Al_4C_3:C$ mixture at 1600°C and 40 MPa. The same authors managed to synthesize Ti_2AlC by reactive hot isostatic pressing[5] of a similar powder blend at 1300°C and 40 MPa, almost removing all traces of secondary phases after an annealing for 30 hours. Another solid-state reaction synthesis method with Ti, Al, and graphite was employed by Kisi et al.,[8] yielding a >99 wt. % pure product. An identical starting composition to that of Barsoum et al.[5,7] was used by Gauthier-Brunet et al.[10] They proceeded by reactive sintering between 570°C and 1400°C for 1 hour of a high pressure cold-compacted mixture, eventually having TiC impurities in the as-synthesized product. By means of pressureless sintering, Benitez et al.[11] obtained high purity Ti_2AlC along with TiAl, TiC, and Al_2O_3 ancillary phases, using Ti, Al, and TiC as reactants. The same approach was used by Zhou et al.[12] with fine commercial Maxthal® Ti_2AlC powder. Elemental powders of Ti, Al, and C have been used in various other routes, such as arc melting[14] or SHS.[15-18] Ti-aluminides and TiC were always found in the final product. A maximum yield of 99.7% of Ti_2AlC and Ti_3AlC_2 was obtained by Hendaoui et al.[16] after a mechanical activation of elemental powders and additions of excess Al. As mentioned earlier, these techniques lead to bulk dense samples, necessitating additional high-energy pulverization means to end up with a powdered product. Ti_2AlC produced by proprietary methods developed by 3-ONE-2[20] and Kanthal AB[21,22] also contained non-negligible amounts of impurities, knowing TiC, TiAl, and $Ti_{1.2}Al_{0.8}$.

Recently, Ti_2AlC was synthesized by Galvin et al.[19] using a molten salt method. They separately used NaCl, KCl, and a NaCl/KCl mixture as synthesis medium. They reached a maximal purity of 88 wt. % Ti_2AlC, when performing the experiment at 1000°C in argon for 5 hours and using the NaCl/KCl mixture. The as-synthesized Ti_2AlC was recovered by grinding with mortar and pestle and washing out the salt with water.

The molten salt shielded synthesis (MS^3) method described elsewhere[23] can be considered as an efficacious alternative to synthesis techniques mentioned earlier. A gas-tight salt encapsulation enables experiments to be conducted in air and at lower temperatures than conventional synthesis routes—commonly employing protective atmospheres such as argon—hence reducing processing costs. In addition, pure (>96 wt. %) and homogeneous MAX phase powders can be obtained and the technique yielded promising results for the synthesis of Ti_3SiC_2.[24] The inter-diffusion of elements in the menstruum of molten salt is enhanced and the recovery of the final product is done through a simple water-based leaching step, without additional milling steps. The finely granulated powder can be further processed into desired components via conventional ceramic processing.

For reasons mentioned above, Ti_2AlC has high potential for uses in oxidizing environments. It naturally forms a protective Al_2O_3 scale, limiting the diffusion rate of oxygen and therefore slowing down further material consumption.[25] Differences in oxidation kinetics are found in literature due to the discrepancies in microstructural features. Large grains (>10 μm) indeed promote parabolic to linear oxidation behavior,[26-28] while cubic or power law fitted kinetics are usually observed for fine-grained (between 1 and 10 μm) microstructures.[28,29] However, the influence of surface quality on oxidation is not documented so far. To the best of the authors' knowledge, only one study[30] mentioned about breakaway oxidation of damaged surfaces and fast buildup of large intertwined rutile crystals. Nevertheless, further studies about the relation between surface quality and oxidation response are required to understand the behavior of the material in harsh environments.

In this work, Ti_2AlC powder synthesized by MS^3 was densified by following two approaches, pressureless sintering (PS) and field-assisted sintering technology/spark plasma sintering (FAST/SPS). The samples with the highest density were used for oxidation experiments. Prior to oxidation, their surfaces were prepared using three degrees of finishing, viz., polishing to 50 nm silica suspension, grinding with grit size P80 SiC abrasive paper and sandblasting with F36 Al_2O_3 particles. Oxide growth was essentially correlated with the initial surface roughness.

2 | EXPERIMENTAL PROCEDURE

2.1 | Material synthesis

Ti_2AlC powder was synthesized by the MS^3 method, following a similar procedure as elsewhere.[23] Briefly, elemental powders of Ti (−325 mesh, 99.5%, Alfa Aesar), Al (−325 mesh, 99.5%, Alfa Aesar) and graphite (APS 7-11 μm, 99%, Alfa Aesar) were mixed in different molar proportions as showed in Table 2. KBr (99%, Alfa Aesar) powder was mixed with the starting precursors in a 1:1 weight ratio. The

TABLE 2 Phase purity outcomes obtained with different synthesis parameters (temperature, stoichiometry, holding time)

Sample Nomenclature	Temperature (°C)	Holding time (h)	Stoichiometry Ti:Al:C	Detected phases (mass fraction)
TAC-1	950	5	2:1:1	Ti_2AlC (83%), Ti_3AlC_2 (13%), TiC (3%), Ti[a]
TAC-2	1000	5	2:1:1	Ti_2AlC (83%), Ti_3AlC_2 (17%)
TAC-3	1050	5	2:1:1	Ti_2AlC (73%), Ti_3AlC_2 (27%)
TAC-4	1000	1	2:1:1	Ti_2AlC (41%), TiAl (24%), TiC (23%), Ti_3Al (8%), C (4%)
TAC-2	1000	5	2:1:1	Ti_2AlC (83%), Ti_3AlC_2 (17%)
TAC-5	1000	10	2:1:1	Ti_2AlC (75%), Ti_3AlC_2 (25%)
TAC-6	1000	15	2:1:1	Ti_2AlC (75%), Ti_3AlC_2 (25%)
TAC-7	1000	5	2:1:0.8	Ti_2AlC (90%), Ti_3Al (3%), TiAl (3%), TiC (2%), Ti (2%)
TAC-8	1000	5	2:1:0.9	Ti_2AlC (91%), Ti_3AlC_2 (6%), Ti (2%), TiC[a]
TAC-9	1000	5	2:1:0.95	Ti_2AlC (82%), Ti_3AlC_2 (13%), Ti (3%), TiC (2%)
TAC-2	1000	5	2:1:1	Ti_2AlC (83%), Ti_3AlC_2 (17%)
TAC-10	1000	5	2:1.05:1	Ti_2AlC (82%), Ti_3AlC_2 (16%), $TiAl_3$ (2%)
TAC-11	1000	5	2:1.1:1	Ti_2AlC (67%), Ti_3AlC_2 (23%), $TiAl_3$ (5%), Ti_2Al_5 (4%), Ti[a]

[a]Indicates the presence of non-negligible traces.Minute amounts (<1%) of KBr, Al_2O_3, and free carbon were detected in all samples. TAC-2 is the reference batch.

raw materials were mixed in ethanol using zirconia balls (Ø 5 mm) and a 3D shaker mixer (Turbula, Willy A. Bachofen AG, Switzerland) for 24 hours. Afterward, the mixture was dried in a rotary evaporator (Rotavapor R-215, BÜCHI Labortechnik AG, Switzerland) at 70°C, followed by sieving through a 300 μm sieve.

The dried mixture was compacted into 20-mm diameter pellets at 200 MPa with a uniaxial hand press (PW 10, P/O/Weber GmbH, Germany).

The samples were placed in a cylindrical alumina crucible, which was subsequently filled with KBr. The alumina crucibles were heated in a high-temperature furnace (HT 32/17, Nabertherm GmbH, Germany) in air at a rate of 5°C/min with different holding times at peak temperatures from 950°C to 1050°C, as indicated in Table 2. Beyond cooling, the crucible was washed with hot water to remove the salt. Vacuum filtration of Ti_2AlC powder was carried out with boiling deionized water and ethanol to further reduce the salt content. Finally, the powder was dried at 70°C and passed through a 25 μm sieve.

The influence of three process temperatures (950°C, 1000°C and 1050°C), four holding times (1, 5, 10, and 15 hours) and different Ti:Al:C stoichiometries (2:1:1, 2:1.1:1, 2:1.05:1, 2:1:0.8, 2:1:0.9, and 2:1:0.95) on phase composition were investigated (Table 2).

2.2 | Material processing

Sintering studies and densification were performed using the optimized composition (2:1:0.9, 1000°C, 5 h, particle size <25 μm). Ti_2AlC was consolidated using two different techniques: pressureless sintering (PS) and field-assisted sintering technology/spark plasma sintering (FAST/SPS). For PS, green compacts (Ø 13 mm) were pressed at

200 MPa in a steel die using a uniaxial press (PW 10, P/O/Weber GmbH, Germany). Densification was carried out in a vacuum chamber furnace (HTK 25 Mo/16-1G Ar, Gero Hochtemperaturöfen GmbH, Germany), under argon atmosphere. The samples were heated up to maximal temperatures of 1300°C and 1400°C at a rate of 5°C/min with an isothermal holding time of 3 hours. For FAST/SPS, as-synthesized Ti_2AlC powder was pre-compacted at 50 MPa in a graphite die (inner diameter of 20 mm). Graphite foil was used between powder and graphite die/punches to enable mechanical, electrical and thermal contact during sintering as well as to prevent reactions between the die and Ti_2AlC. The die was additionally lined with a carbon felt for better thermal insulation. The Ti_2AlC powder was densified in a FAST/SPS furnace (FCT-HPD5, FCT Systeme GmbH, Germany) at a heating rate of 100°C/min up to 1200°C and 50 MPa uniaxial pressure in vacuum (~4 mbar). The pressure was applied at the beginning of the sintering cycle, before heating. The samples were hold at the maximal temperature and pressure for 10, 30, and 60 minutes. Temperature was monitored using an axial pyrometer, which was focused on the surface of the upper drilled punch, close to the specimen. Samples were ground after densification to remove the remainder of graphite foil.

For microstructural analysis, samples were cut, mounted, ground, and polished to a 50 nm colloidal silica suspension (OP-S, Struers ApS, Denmark).

A pellet sintered by FAST/SPS was cut into three portions using a diamond-studded wire saw. The first portion was ground with P80 silicon carbide (SiC) abrasive paper, meanwhile the second sample was sandblasted (MHG Strahlanlagen GmbH, Germany) at a pressure of 4 bar with coarse F36 (420-595 μm) Al_2O_3 particles. The third part was ground with P4000 SiC paper, followed by diamond polishing (3 and 1 μm) and eventually polished with OP-S. All three parts were oxidized in static air in a high-temperature furnace (HTC 03/15, Nabertherm GmbH, Germany) at a rate of 10°C/min until 1200°C, and kept at this temperature for 50 hours.

2.3 | Material characterization

Particle size distribution (PSD) of the Ti_2AlC powders was measured by laser diffraction (Horiba LA950-V2, Retsch GmbH, Germany). Phase composition of the synthesized powders and consolidated samples were determined by X-ray diffraction (XRD) using a Bragg-Brentano diffractometer in θ-2θ geometry (D4 Endeavor, Bruker AXS GmbH, Germany). The scans were conducted with a step size of 0.02° 2θ and a step time of 0.75 seconds in the 2θ = 5°-80° range. Diffractograms were plotted in the 2θ = 7°-80° range. Qualitative phase analysis was performed with the HighScore Plus 3.0.5 software (PANalytical BV, Netherlands). Rietveld refinement was done with TOPAS V4 (Bruker AXS GmbH, Germany). Titanium, aluminum, and potassium contents were determined using inductively coupled plasma optical emission spectrometry (ICP-OES, iCAP 7600, Thermo Fisher Scientific, USA), meanwhile carbon and oxygen contents were analyzed using carbon/sulfur and nitrogen/oxygen/hydrogen-determinators (CS600 and TCH600, Leco Instrumente GmbH, Germany), respectively.

Morphology of as-synthesized powder particles, microstructure of bulk samples, cross-sections and fracture surfaces were observed using scanning electron microscopy (SEM, Zeiss Ultra55 and Zeiss Crossbeam 540, Carl Zeiss AG, Germany). In addition, elemental composition was characterized by energy-dispersive X-ray spectroscopy (EDS), which is attached to the SEM. Grain size and morphology were characterized using electron backscatter diffraction (EBSD-Camera, Nordlys II, EBSD-Software, Aztec, Oxford Instruments, United Kingdom) coupled to SEM (Zeiss Merlin, Carl Zeiss AG, Germany). Crystal structures were retrieved from the Inorganic Crystal Structure Database (ICSD).

Bulk and absolute densities of green compacts and sintered samples were determined using mass-volume measurements and volume displacement by Archimedes' principle respectively. Based on these results, on Rietveld refinement and on values of theoretical density, relative density of multiphase specimen was estimated using the rule of mixture. Porosity of pressureless-sintered samples was determined by image analysis using the Fiji package of the ImageJ software. The degree of preferred orientation (η) of raw powders and sintered samples was calculated after determining the March-Dollase parameter (r) with the TOPAS software. The following formula (Equation 1) was used[31]:

$$\eta = 100\,\% \left[\frac{(1-r)^3}{1-r^3} \right]^{1/2}. \quad (1)$$

Surface roughness of parts intended for oxidation experiments was characterized using a noncontact profilometer (cyberSCAN CT 350T, cyberTECHNOLOGIES GmbH, Germany) equipped with a chromatic sensor head (CHRocodile E1000, Precitec Optronic GmbH, Germany). Surfaces (~4 mm × 4.5 mm) were analyzed with a scan step size of 50 μm in x-direction and increments of 1 μm in y-direction. Arithmetical mean roughness (R_a), root mean squared roughness (R_q), mean roughness depth (R_z), and maximum roughness depth (R_{max}) were determined using the SCAN CT 8.10 surface metrology software.

Thermogravimetric analysis (TGA) was performed in a high-temperature silicon carbide furnace (STA 449 F1, Netzsch GmbH, Germany) in the same conditions as the oxidation experiments and the data analyzed with the

Proteus® software. Parabolic and cubic fitting was performed using the equations relating the mass gain per unit area, the corresponding rate constants and the oxidation time[28] and the R^2 values were determined to estimate goodness-of-fit.

3 | RESULTS AND DISCUSSION

3.1 | Synthesis

Three synthesis parameters were varied independently, temperature, composition, and holding time (Table 2). At first, the maximal temperature was optimized with values between 950°C and 1050°C, keeping the stoichiometry and holding time constant. The sample predominantly contained Ti_2AlC for all the temperatures (Figure 1A), although the diffractograms revealed the presence of secondary phases such as Ti_3AlC_2, TiC, unreacted Ti and residual graphite. KBr is also detected in low amounts in all samples (most visible at $2\theta = 27°$ and $2\theta = 47.7°$), being entrapped within uncrushed hard agglomerates. The main peak of graphite (002) overlaps with KBr (200). The remainder of Ti reacted at higher temperature ($T \geq 1000°C$), and its reflection (101) at $2\theta = 40.1°$ disappeared on the corresponding diffractograms. The fraction of Ti_3AlC_2 gradually increased with temperature due to the reactions between Ti_2AlC and TiC. As stated by Wang et al.,[32] three nonoverlapping peaks ($2\theta = 9.5°$ for Ti_3AlC_2 (002), $2\theta = 13°$ for Ti_2AlC (002) and $2\theta = 35.9°$ for TiC (111)) can be considered in order to have a first estimation of phase composition. Rietveld refinement corroborated the presence of 83 wt. % Ti_2AlC, 13 wt. % Ti_3AlC_2, 3 wt. % TiC, and traces of Ti at 950°C (Table 2). The expected formation mechanisms of Ti_2AlC resemble reactions proposed in literature,[10,33] but do not unequivocally constitute an evidence of each product formation via the molten salt based synthesis route. Differential thermal analysis (DTA) was conducted but not included in the present work, as the detected signal generally vanished in the background noise and made peak assignment arduous. It is believed that the reaction pathway follows two regimes, one being the classical powder metallurgical synthesis before the melting point of KBr, the second being dictated by diffusion of species in the molten salt and accelerated kinetics of reaction. A solid-state reaction between Ti and C is expected before reaching the melting point of Al (Equation 2). Fan et al.[34] reported the formation of a thin sub-stoichiometric TiC shell on Ti particles by solid-state diffusion of C. At ~660°C, Al reached its melting point (Equation 3), surrounding discrete particles of graphite and Ti. Diffusion of elements in the melt is enhanced and compounds are essentially formed via solid-liquid reaction. Type-I aluminides,[35] TiAl and Ti_3Al, nucleated on Ti particles (Equations 4 and 5). Gauthier-Brunet et al.[10] reported the formation of Ti_3Al layers around Ti particles in the case of reactive sintering. Školáková et al.[36] demonstrated that Ti particles were surrounded with Ti_3Al, TiAl, as well as aluminum rich $TiAl_2$ and $TiAl_3$ phases in the case of reactive sintering of a mixture of Ti and Al at 700°C for 20 minutes. In our case at this range of temperature, KBr is still in a solid state.

$$Ti_{(s)} + xC_{(s)} \rightarrow TiC_{x(s)} \quad (2)$$

$$Al_{(s)} \rightarrow Al_{(l)} \quad (3)$$

$$Ti_{(s)} + Al_{(l)} \rightarrow TiAl_{(s)} \quad (4)$$

$$3Ti_{(s)} + Al_{(l)} \rightarrow Ti_3Al_{(s)} \left(-22.6\,kJ.mol^{-1} < \Delta G_5^0 < -21.2\,kJ.mol^{-1}\right) \quad (5)$$

At 735°C, KBr reached its melting point, enveloping the remainder of molten Al, graphite, unreacted Ti, TiC-, and Ti_xAl-templated Ti particles. As expected in a molten salt process, atomic diffusion is enhanced by the presence of a liquid media. Quenching performed with a Ti-Si-C system[24] and molten salt diffusion experiments with pure Ti[23] showed that large diffusion spheres were present around elements from

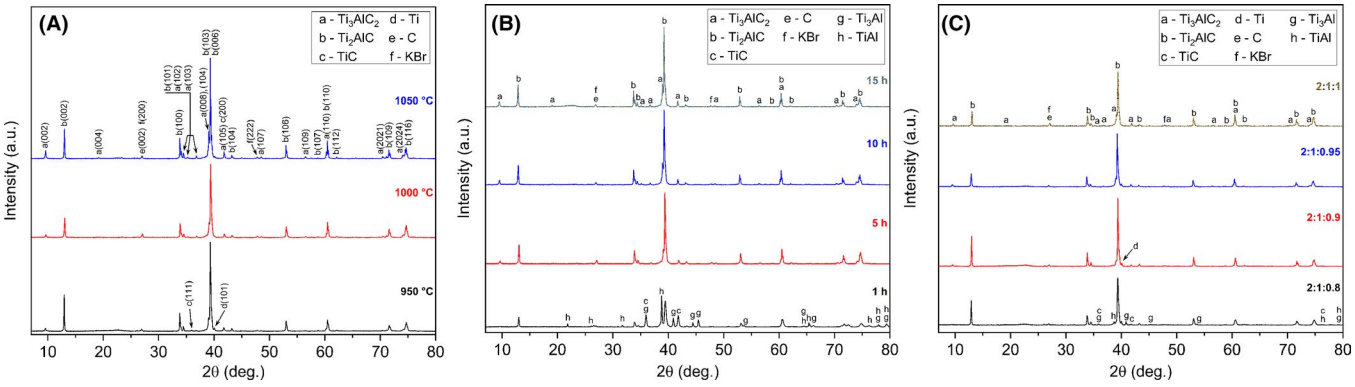

FIGURE 1 XRD diffractograms obtained with different parameter sets: (A) T = 950-1050°C, molar ratio 2:1:1, t = 5 h, (B) T = 1000°C, molar ratio 2:1:1, t = 1-15 h, (C) T = 1000°C, molar ratio 2:1:x with $0.8 \leq x \leq 1$, t = 5 h [Color figure can be viewed at wileyonlinelibrary.com]

the starting materials and that elements diffused deeply into the molten salt. It suggests a high solubility of Ti in molten KBr. The dissolution of graphite in titanium aluminides was reported in the 800-900°C range for reactive sintering[10]. In a molten salt medium though, it is unlikely that graphite dissolves and the process is believed to be based on a "template growth" scheme as reported by Liu et al. for TiC coatings on graphite flakes.[37] The formation of the intermediate Ti_3AlC phase (Equation 6) can be expected in the present work, but through a different mechanism. However, its presence was not evidenced.

$$Ti_3Al_{(s)} + C_{(s)} \rightarrow Ti_3AlC_{(s)} \; (-83.8\,kJ.mol^{-1} < \Delta G_6^0 < -67.4\,kJ.mol^{-1}) \quad (6)$$

This phase was found to be stable up to 1200°C during reactive sintering.[10] However, in the present work, Ti_3AlC may have reacted in its entirety with C and Ti-Al intermetallic compounds before 950°C (Equations 7), since no peaks attributed to this phase were observed on the corresponding diffractogram (Figure 1A). The reduction of reaction temperatures is enabled by the presence of the KBr melt and the improved solid-liquid diffusion in this medium, hence reaction kinetics are different from solid-state synthesis. In fact, the formation of Ti_2AlC at 900°C was already reported by Galvin et al.[19] for a molten salt synthesis process in argon.

$$Ti_3AlC_{(s)} + C_{(s)} \rightarrow Ti_2AlC_{(s)} + TiC_{(s)} \; (-183\,kJ.mol^{-1} < \Delta G_{7A}^0 < -175\,kJ.mol^{-1}) \quad (7A)$$

$$Ti_3AlC_{(s)} + C_{(s)} \rightarrow Ti_3AlC_{2(s)} \; (-12\,kJ.mol^{-1} < \Delta G_{7B}^0 < -10\,kJ.mol^{-1}) \quad (7B)$$

At 1000°C, the composition was essentially biphasic (83 wt. % Ti_2AlC, 17 wt. % Ti_3AlC_2). Ti_2AlC may have further reacted with TiC to form Ti_3AlC_2 according to Equation 8. This reaction occurred at lower temperature than reported.[10] The possibility of a peritectic reaction between TiC_x and liquid Ti-aluminides as reported by Khoptiar et al.[18] for SHS is dismissed. The reaction temperature reached in the present work is far below the melting point of these intermetallics. At 1050°C, the content of Ti_3AlC_2 increased at the expense of Ti_2AlC. In fact, an increase of 50°C in the process temperature caused a decrease of 10% in the Ti_2AlC content.

$$Ti_2AlC_{(s)} + TiC_{(s)} \rightarrow Ti_3AlC_{2(s)} \; (\Delta G_8^0 = +165\,kJ.mol^{-1}) \quad (8)$$

Standard free energies of reaction were calculated in the 1000-1273 K range for Equations (5), (6), (7A), (7B) and (8) according to data found in literature,[38-40] and yielded negative values for (5), (6), (7A), and (7B) but positive for (8). It appears that Equation 8 may not be thermodynamically favorable, and that the formation of Ti_3AlC_2 may originate from Equation 7B instead.

Thus, below 1000°C, reactions were not completed and residual TiC, Ti, and C were detected. At 1000°C, the composition was essentially biphasic and samples predominantly contained Ti_2AlC and Ti_3AlC_2. Above 1000°C, phase transformation started to occur, hence a reduction in Ti_2AlC purity was noticed. Therefore, the intermediate temperature of 1000°C was considered as a good compromise to maintain a high Ti_2AlC phase purity, without having detrimental impurities for oxidation experiments.

Furthermore, the holding time was optimized, fixing the other parameters at 1000°C for the maximal temperature and 2:1:1 for the molar ratio. Figure 1B displays XRD patterns of samples held for 1, 5, 10, and 15 hours. For the shortest holding time, intermetallics (TiAl, Ti_3Al) and TiC were present in considerable amounts due to incomplete reactions between raw materials, representing over half the weight fraction of the sample (Table 2). Presence of TiC and aluminides were also reported for short dwell times (2 hours), and an increase to 5 hours promoted formation of more Ti_2AlC.[19] The absence of Ti_3AlC suggests that formation kinetics of Ti_3AlC and Ti_2AlC are probably much different. Gauthier-Brunet et al.[10] assumed a slow and fast formation of former (Equation 6) and latter (Equation 7A) phases, respectively. Additionally, no peak for Ti_3AlC_2 was evidenced for an 1 hour dwell time, pointing out slow formation kinetics for this phase too (Equation 7B). Increasing the holding time to 5 hours promoted the reaction of Ti-aluminides, TiC and remaining graphite to form additional Ti_2AlC and Ti_3AlC_2 phases. The characteristic strong reflections of both phases appeared and overlapped over the $2\theta = 38\text{-}40°$ range. Longer holding times generated an increasing percentage of Ti_3AlC_2, visible through a slight dissociation of Ti_3AlC_2 (008) and Ti_2AlC (006) in the above mentioned 2θ range and a decrease in the Ti_2AlC (002) to Ti_3AlC_2 (002) peak intensity ratio.

Thus, short holding times were not suitable for completion of reactions. After 1 hour, the amount of impurities was substantial. After 5 hours, the composition was mainly biphasic and samples predominantly contained Ti_2AlC and Ti_3AlC_2. After 10 hours, the amount of Ti_2AlC decreased by 8%, as a result of gradual phase transformation, even though Ti_2AlC and Ti_3AlC_2 were still the only two detected phases. Thereby, an optimal holding time of 5 hours was retained.

Finally, the third parameter was optimized, where both Al and C contents were varied alternately (Figure 1C and Table 2), keeping the temperature and holding time constant according to former optimization. The stoichiometric sample served as reference. Sub-stoichiometric carbon contents as well as minor excesses of Al were investigated. Al hyper-stoichiometries were reported by various authors[16,41,42] as a way to promote reactions between TiC and intermetallics and to counterbalance losses of high vapor pressure A-element during the synthesis of Al MAX phases. A carbon-deficient stoichiometry of 2:1:0.8 suppressed the formation of Ti_3AlC_2. Reflections of Ti-aluminides, TiC as well as unreacted Ti were observed. Carbon deficiency limited the overall reaction, though unreacted graphite was still

observed after magnifying XRD diffractograms in the specific 2θ range. High content of Ti_2AlC (90 wt. %, Table 2) suggested fast completion of Equation 7A. However, remaining Ti showed that Equation 2 was limited by the lack of graphite. At a molar ratio of 2:1:0.9 the intermetallic phases reacted. The content of TiC was strongly reduced and detected as traces, meanwhile presence of unreacted Ti was still evidenced. The maximum Ti_2AlC and MAX phase ($Ti_2AlC + Ti_3AlC_2$) yields were achieved (91 wt. % and 97 wt. % respectively). At a molar ratio of 2:1:0.95, contents of Ti_3AlC_2 and TiC increased to the expense of the Ti_2AlC MAX phase. An increase in the Al content (not shown on diffractograms) did not lead to higher Ti_2AlC phase purity (Table 2). The excess of Al is confined in the salt bed during MS[3], hence losses of A-element are not expected, unlike during conventional synthesis routes. Al-rich intermetallic compounds, such as titanium trialuminide ($TiAl_3$) and Ti_2Al_5 were evidenced. Ti-rich compounds (TiAl and Ti_3Al) were not detected. Their free energies of formation are higher than that of $TiAl_3$ for the considered temperature range.[35] The formation of $TiAl_3$ can be given by Equation 9. Ti_2Al_5 is known to require TiAl as intermediate product[35] and forms through a series of reactions. Its formation can be explained via Equations 4, 10, and 11.

$$Ti_{(s)} + 3Al_{(l)} \rightarrow TiAl_{3(s)} \quad (9)$$

$$TiAl_{(s)} + Al_{(l)} \rightarrow TiAl_{2(s)} \quad (10)$$

$$TiAl_{3(s)} + TiAl_{2(s)} \rightarrow Ti_2Al_{5(s)} \quad (11)$$

Nevertheless, Školáková et al.[36] found out that Ti_2Al_5 can form far below the melting point of Al when annealing Ti/Al mixtures for 1 day at 450°C or 8 hours at 500°C. This contradicts the fact of Sujata et al.[35] that $TiAl_3$ is found prior to any other titanium aluminide. As reactions in molten KBr salt are drastically accelerated, it may not be overstated that Ti_2Al_5 and subsequently $TiAl_3$ could form the same way as Školáková et al.[36] emphasized, following the scheme described by Equations 12 and 13.

$$2Ti_{(s)} + 5Al_{(l)} \rightarrow Ti_2Al_{5(s)} \quad (12)$$

$$Ti_2Al_{5(s)} + Al_{(l)} \rightarrow 2TiAl_{3(s)} \quad (13)$$

In this way, slight hyper-stoichiometries of Al were not required to compensate A-element losses. They were even detrimental, because of Ti-aluminide formation. For the same reason, high deficiencies in carbon content were not favorable to increase Ti_2AlC purity. The highest yield was obtained with a 10% carbon deficient stoichiometry. Therefore, the Ti:Al:C = 2:1:0.9 stoichiometry was selected for further processing steps.

Traces of Al_2O_3 were detected by powder XRD and confirmed by SEM observations. The oxygen content in elemental raw powders was found to be non-negligible as shown in

TABLE 3 Element analysis of raw materials and as-synthesized Ti_2AlC MAX phase powders (B_1, B_2, and B_3 indicate batch numbers)

	Element content (wt. %)				
Powders	**O**	**K**	**Ti**	**Al**	**C**
Ti	0.855 ± 0.010	-	Balance	-	-
Al	0.420 ± 0.040	-	-	Balance	-
C	0.242 ± 0.003	-	-	-	Balance
TAC-8-B_1	2.399 ± 0.003	0.308 ± 0.005	71.800 ± 0.800	21.800 ± 0.800	7.957 ± 0.012
TAC-8-B_2	1.910 ± 0.090	0.324 ± 0.004	69.700 ± 0.600	22.900 ± 0.300	7.926 ± 0.007
TAC-8-B_3	1.760 ± 0.060	0.509 ± 0.003	69.700 ± 0.500	22.700 ± 0.300	8.010 ± 0.050

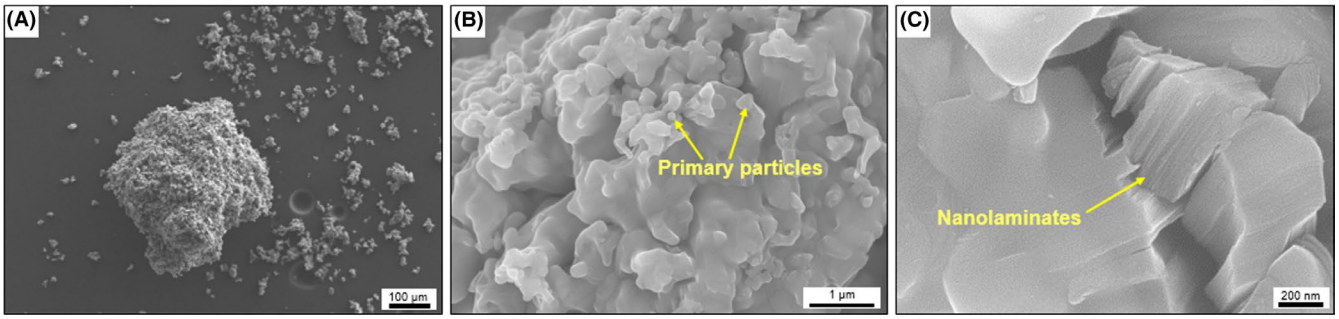

FIGURE 2 Features of Ti_2AlC powder produced by MS[3]: (A) presence of uncrushed hard agglomerates, (B) surface morphology, and (C) nanolaminated structure [Color figure can be viewed at wileyonlinelibrary.com]

Table 3. It was the reason for the presence of alumina after MS[3]. Potassium cations were also detected in minute amounts by ICP-OES, which may be due to the residual amount of KBr present in uncrushed agglomerates.

Secondary electron (SE) SEM images (Figure 2) show features of as-synthesized Ti_2AlC. Figure 2A shows one of these large hard agglomerates contained in the as-synthesized Ti_2AlC powder. The morphology of Ti_2AlC synthesized by MS[3] was rather globular, not acicular like Ti_3AlC_2.[19,27] Galvin et al.[19] reported broad peaks in their XRD patterns and pointed out the presence of nanocrystals. In this work, submicron sized primary particles were also observed (Figure 2B). These primary particles formed larger clusters with smooth surfaces, unlike Ti_3SiC_2 for which the sharp nanolaminated structure has been distinctly seen.[24] Higher magnifications were required to identify individual layers (Figure 2C).

The powder showed a bimodal PSD, with D_{10}, D_{50}, and D_{90} values of 8.4, 18.8, and 54.8 μm, respectively (Figure 3A). A narrow monomodal PSD was achieved using a 500-mesh sieve, attaining D_{10}, D_{50}, and D_{90} values of 7.5, 13.6, and 22.9 μm respectively.

EBSD analyses of cold-compacted as-synthesized Ti_2AlC powders (Figure 4) gave an insight into primary particle size, particle shape, and phases. The phase map (Figure 4B) shows that Ti_2AlC particles are agglomerates of Ti_2AlC nanocrystals with a mean size of ~0.9 μm (Table 4). In addition, isolated grains of Al_2O_3 and Ti_3AlC_2 in small proportions were detected. EBSD images demonstrated that Ti_2AlC particles were composed of a multitude of primary particles and highlighted the fine-grained microstructure of Ti_2AlC synthesized by MS[3]. It is potentially due to multiple nucleation of product phases on particles of elemental reactants assisted by the molten salt during synthesis. Grain size was submicrometric for both Ti_2AlC and Ti_3AlC_2, and average grain aspect ratio was between 1 and 2, indicating a quasi-equiaxed grain morphology (Table 4).

TABLE 4 Grain size and grain aspect ratio outcomes of EBSD analyses for as-synthesized Ti_2AlC powder

Average grain size (μm)		Average grain aspect ratio	
Ti_2AlC	Ti_3AlC_2	Ti_2AlC	Ti_3AlC_2
0.93 ± 0.42	0.66 ± 0.12	1.75 ± 0.52	1.73 ± 0.63

This powder was used for subsequent steps in the present work.

3.2 | Sintering

3.2.1 | Pressureless sintering

Pressureless sintering (PS) of Ti_2AlC in argon was investigated. Bulk green density of cold-compacted bodies was 54% of the theoretical. At 1300°C (Figure 5A), samples (PS-1300) exhibited a relative density of ~70%–75% with a continuous network of large interconnected pores (~20 μm). At 1400°C (Figure 5B), samples (PS-1400) achieved higher relative density (~88%–90% of the theoretical), similar to values mentioned in literature[43,44]. The microstructure of these samples showed a multitude of submicrometer-sized pores scattered between a few larger ones (~5-10 μm). Higher

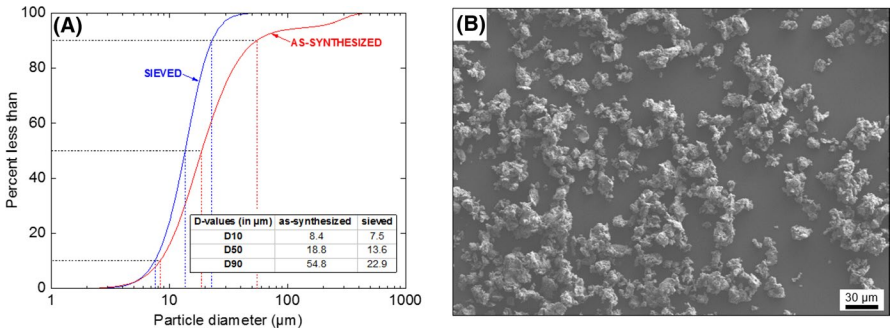

FIGURE 3 Sieving of Ti_2AlC powder produced by MS[3]: (A) volume particle size distributions of as-synthesized and sieved powders, (B) presence of agglomerates homogeneous in size after sieving [Color figure can be viewed at wileyonlinelibrary.com]

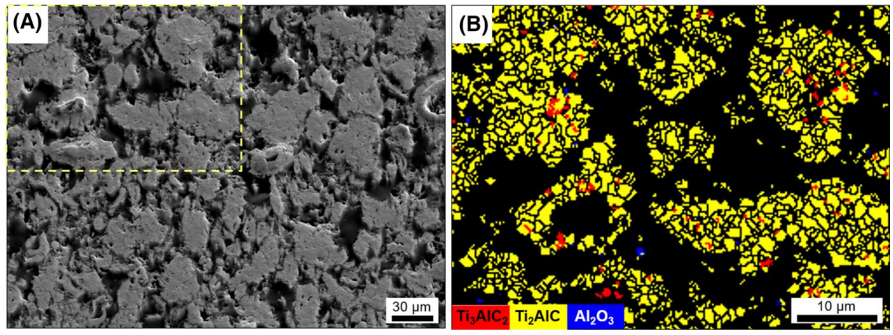

FIGURE 4 EBSD analysis of compacted as-synthesized Ti_2AlC powder: (A) SE image and (B) phase map corresponding to the dashed area [Color figure can be viewed at wileyonlinelibrary.com]

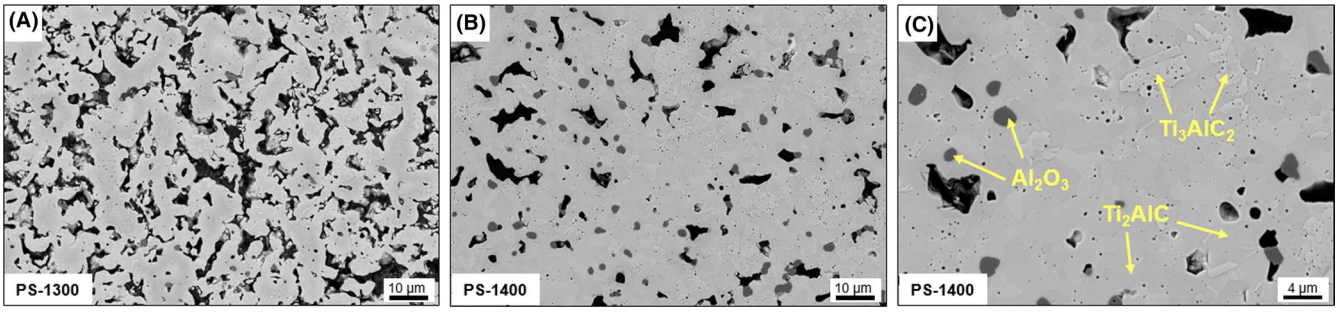

FIGURE 5 Pressureless sintering of Ti_2AlC, 3 h in argon (heating rate: 10°C/min): (A) T = 1300°C, (B) T = 1400°C and (C) T = 1400°C, higher magnification [Color figure can be viewed at wileyonlinelibrary.com]

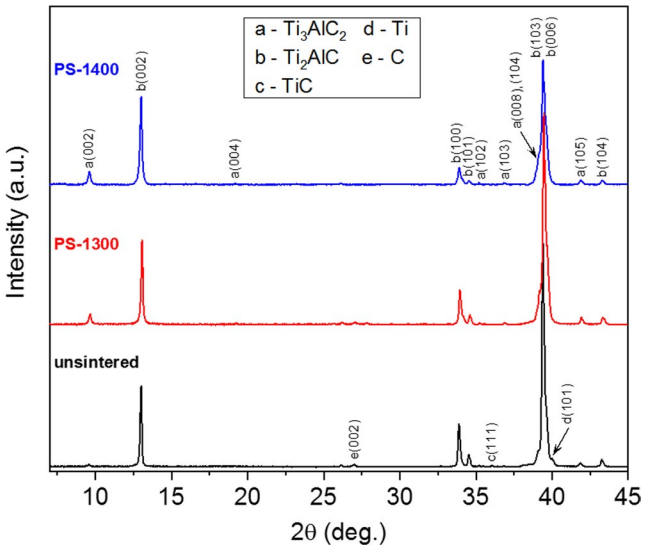

FIGURE 6 XRD diffractograms of pressureless-sintered Ti_2AlC, compared to the unsintered powder [Color figure can be viewed at wileyonlinelibrary.com]

magnification (Figure 5C) showed the presence of needle-shaped grains/clusters of grains of Ti_3AlC_2 confirmed by EDS. The submicrometer-sized pores were predominantly located within clusters of Ti_3AlC_2 grains. Dark-grey Al_2O_3 grains were observed with backscattered electrons (BSE). The sintering atmosphere certainly contained few ppm of oxygen, responsible for local oxidation of Al, though, it is believed that Al_2O_3 was essentially present before PS, as evidenced by the oxygen content in as-synthesized Ti_2AlC powders (Table 3). The observed relief was due to disparate etching of Ti_2AlC and Ti_3AlC_2 MAX phases during the final polishing step. The Al content being higher in Ti_2AlC, it is more predisposed to etching by OP-S than Ti_3AlC_2. The differences in topography between Ti_2AlC and Ti_3AlC_2 were not caused by differences in hardness. Specimen sintered at both temperatures showed a substantial increase in the Ti_3AlC_2 phase content (Figure 6 and Table 5). Rietveld refinement evidenced 81 wt. %, 17 wt. %, and 2 wt. % of Ti_2AlC, Ti_3AlC_2, and Al_2O_3 respectively for PS-1300 samples. The PS-1400 samples contained 78 wt. %, 20 wt. %, and 2 wt. % of Ti_2AlC, Ti_3AlC_2, and Al_2O_3, respectively. Unreacted graphite was gradually consumed (disappearance of the C (002) reflection at 2θ = 27°) and contributed to the formation of Ti_3AlC_2 via mechanisms described above. Additionally, a phenomenon of phase interconversion is believed to occur, as described by Kisi et al.[8] Al planes are thought to slowly diffuse out of Ti_2AlC into TiC. Ti_6C octahedra come close to each other forcing Ti to diffuse out. The Ti_2AlC structure eventually collapses into Ti_3AlC_2.

TABLE 5 Rietveld quantitative phase analysis and density of pressureless-sintered Ti_2AlC

Sample	Detected phases (mass fraction)	Density (% of TD)
unsintered (raw powder)	Ti_2AlC (91%), Ti_3AlC_2 (6%), Ti (2%), TiC[a],C[a]	54
PS-1300	Ti_2AlC (81%), Ti_3AlC_2 (17%), Al_2O_3 (2%)	70-75
PS-1400	Ti_2AlC (78%), Ti_3AlC_2 (20%), Al_2O_3 (2%)	88-90

[a]Indicates the presence of traces. Density is given as compared to the theoretical density (TD).

As a result, full densification of Ti_2AlC without any alteration cannot be attained by pressureless sintering. Consequently, an electric field/pressure assisted sintering technique was employed in order to rapidly reach near full densification with minimal purity degradation.

3.2.2 | FAST/SPS

Ti_2AlC powders were sintered by FAST/SPS at lower temperatures (1200°C) than PS under a pressure of 50 MPa in vacuum. For reasons mentioned in the section above, aim was to achieve near full densification by concomitantly limiting phase transformation. A higher heating rate (100°C/min) as compared to PS was used. The onset of densification was around 800-850°C, and the specimen (Figure 7A) exhibited higher relative density (98.5% of the theoretical) after a 10 minutes dwell time at

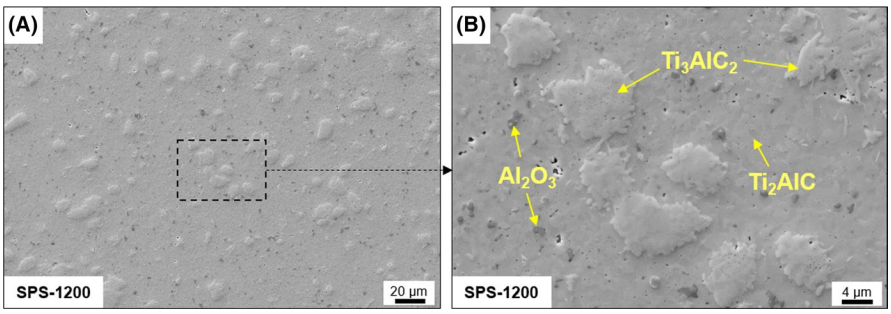

FIGURE 7 SPS of Ti_2AlC at 50 MPa, 10 min in vacuum (heating rate: 100°C/min): (A) T = 1200°C, (B) T = 1200°C, magnified area [Color figure can be viewed at wileyonlinelibrary.com]

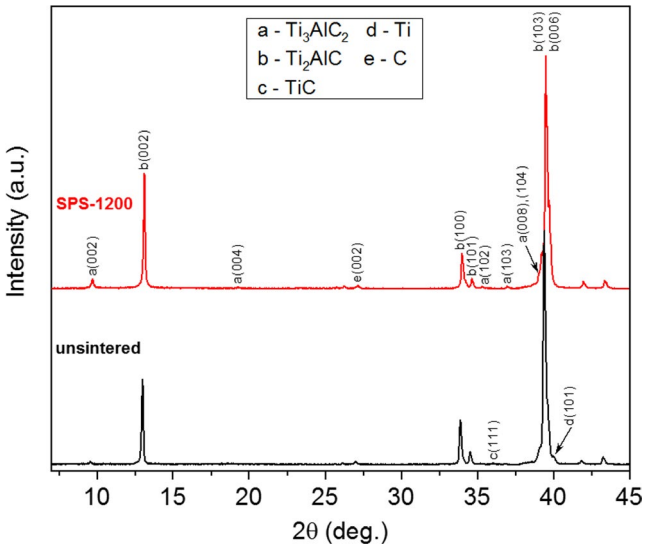

FIGURE 8 XRD diffractograms of „SPSed" Ti_2AlC, compared to the unsintered powder [Color figure can be viewed at wileyonlinelibrary.com]

1200°C, with pore size below 5 µm. Topographical differences were also observed due to different chemical etching of Ti_2AlC and Ti_3AlC_2 phases during the final polishing step. On account of denser microstructures, clusters of Ti_3AlC_2 grains were more discernable on SEM images of SPS-1200 samples (Figure 7B). They were ~10-20 µm in size. Less phase transformation (Figure 8 and Table 6) was observed as compared to PS samples due to the shorter sintering times, slightly reducing the extent to which Ti_3AlC_2 is formed. Quantitative phase analysis evidenced 84 wt. %, 14 wt. %, and 2 wt. % of Ti_2AlC, Ti_3AlC_2, and Al_2O_3, respectively. Traces of unreacted Ti present in as-synthesized Ti_2AlC were entirely consumed (disappearance of the Ti (101) reflection at $2\theta = 40.1°$), contributing to the formation of Ti_2AlC and Ti_3AlC_2. The TiC (111) reflection at $2\theta = 35.9°$, hardly discernable for Ti_2AlC powder (unsintered sample), was not evidenced after SPS. It was consumed during sintering, proving that the remainder of unreacted Ti did not promote the formation of additional TiC. However, minute amounts of free carbon were still detectable. A non-negligible amount of Al_2O_3 was detected in SPS-1200, as for PS. The degree of preferred orientation was 7.37 for SPS-1200, indicating a slight texturing.

EBSD analyses (Figure 9) gave an insight into grain size, grain shape and phases of SPSed samples. The previously observed relief, also appearing on Figure 9A, are either single grains of Al_2O_3 or clusters of Ti_3AlC_2, as displayed on the phase map (Figure 9B). Ti_2AlC produced by MS[3] and sintered by FAST/SPS showed a submicron fine-grained microstructure. Grain sizes of the three phases are below 1 µm (Table 7), indicating that sintering by FAST/SPS did not promote grain growth. Increasing holding times had no influence on grain growth and the microstructure remained the same after one hour of sintering. To the authors' best knowledge, it is the smallest grain size reported so far for Ti_2AlC. For instance, direct synthesis of Ti_2AlC by FAST/SPS of elemental

TABLE 6 Rietveld quantitative phase analysis and density of "SPSed" Ti_2AlC

Sample	Detected phases (mass fraction)	Density (% of TD)	March-Dollase parameter (r)	Degree of preferred orientation (η)
Unsintered (raw powder)	Ti_2AlC (91%), Ti_3AlC_2 (6%), Ti (2%), TiC[a],C[a]	54	1[b] 1[c]	→ 0[b] → 0[c]
SPS-1200	Ti_2AlC (84%), Ti_3AlC_2 (14%), Al_2O_3 (2%), C[a]	98.5	0.88[b] 1[c]	7.37[b] → 0[c]
PS-1300	Ti_2AlC (81%), Ti_3AlC_2 (17%), Al_2O_3 (2%)	70-75	N/A N/A	N/A N/A
PS-1400	Ti_2AlC (78%), Ti_3AlC_2 (20%), Al_2O_3 (2%)	88-90	N/A N/A	N/A N/A

[a]Indicates the presence of traces.

[b]measured for Ti_2AlC (002).

[c]measured for Ti_3AlC_2 (002). Density is given as compared to the theoretical density (TD). Values for PS samples are indicated for comparison.

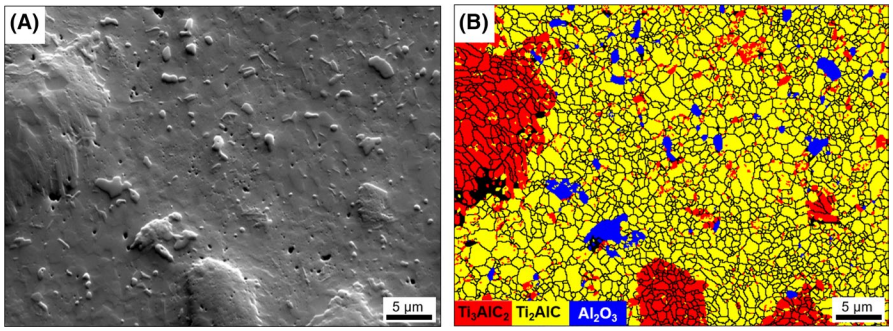

FIGURE 9 EBSD analysis of "SPSed" Ti_2AlC: (A) SE image and (B) corresponding phase map [Color figure can be viewed at wileyonlinelibrary.com]

TABLE 7 Grain size and grain aspect ratio outcomes of EBSD analyses for three samples sintered by SPS for 10, 30, and 60 min, respectively

	Average grain size (µm)			Average grain aspect ratio		
	Ti_2AlC	Ti_3AlC_2	Al_2O_3	Ti_2AlC	Ti_3AlC_2	Al_2O_3
TAC-SPS-10	0.75 ± 0.34	0.62 ± 0.30	0.70 ± 0.37	1.62 ± 0.46	1.85 ± 0.65	1.58 ± 0.43
TAC-SPS-30	0.78 ± 0.36	0.60 ± 0.31	0.62 ± 0.28	1.64 ± 0.48	1.96 ± 0.69	1.50 ± 0.33
TAC-SPS-60	0.79 ± 0.36	0.64 ± 0.30	0.74 ± 0.36	1.62 ± 0.49	1.85 ± 0.65	1.47 ± 0.34

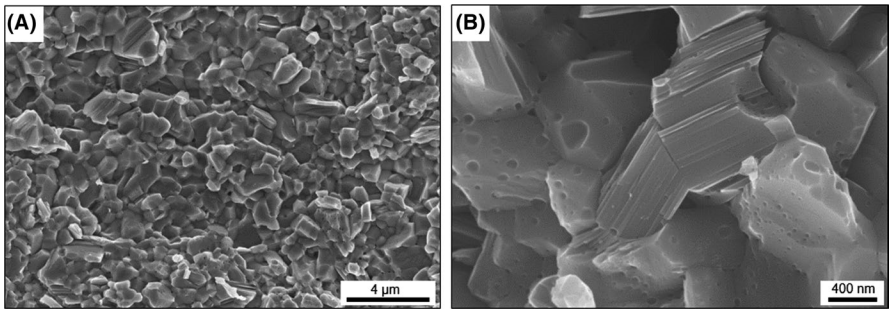

FIGURE 10 Fractographic analysis of Ti_2AlC densified by SPS: (A) insight into the fine-grained microstructure and (B) required high magnification in order to evidence the layered structure

reactants at 1100°C and 30 MPa in vacuum, using a heating rate of 80°C/min and a dwell time of one hour, yielded large elongated grains of 20 µm by 5 µm[41]. Another work[13] based on FAST/SPS of TiAl-carbon nanotube powder at 1200°C and 160 MPa in vacuum produced coarse grains as well (>10 µm according to SEM images). The average aspect ratio of Ti_2AlC grains was close to 1.6 (Table 7), indicating a more symmetrical nature than for Ti_3AlC_2 grains. Longer holding times had no influence on grain aspect ratio either. Al_2O_3 grains were in the same size range. The average aspect ratio was closer to that of Ti_2AlC. Al_2O_3 grains, when not spherical, had a more equiaxed morphology as compared to both Ti_2AlC and Ti_3AlC_2 grains.

Fractured surfaces (Figure 10A) confirmed the fine-grained microstructure evidenced with EBSD analysis. Higher magnifications (Figure 10B) were required to visualize single MAX phase layers and mesopores.

Thereby, FAST/SPS turned out to be a rapid sintering method to enable near full densification of Ti_2AlC powders with 10 minutes of dwell time at 1200°C. At the same time, phase transformation/conversion was limited and original grain size was retained, which are important features for good oxidation resistance.[28]

TABLE 8 Surface roughness of polished, ground and sandblasted Ti_2AlC before oxidation. Values for polished and ground samples are indicated with a cut-off wavelength λ_c = 250 µm and for sandblasted samples with a cut-off wavelength λ_c = 800 µm. R_a = arithmetical mean roughness, R_q = root mean squared roughness, R_z = mean roughness depth, R_{max} = maximum roughness depth

Samples	R_a (µm)	R_q (µm)	R_z (µm)	R_{max} (µm)
Polished (OPS)	0.09 ± 0.01	0.12 ± 0.01	0.77 ± 0.08	0.96 ± 0.15
Ground (P80)	1.18 ± 0.14	1.46 ± 0.18	6.23 ± 0.74	8.33 ± 1.96
Sand blasted (F36)	3.26 ± 0.40	4.05 ± 0.50	19.42 ± 4.37	24.77 ± 19.34

3.3 | Oxidation

Ti_2AlC samples were oxidized at 1200°C in static air for 50 hours, at a rate of 10°C/minute. The temperature was selected according to other works.[3,30,45,46] Most oxidation studies of Al-MAX phases have been based on polished surfaces. The effect of surface quality was therefore studied, by means

of three degrees of finishing, to wit, polished (OPS), ground (P80), and sandblasted (SB) samples.

In this work, the extent to which oxides grew on the specimen's surface was correlated with roughness. The different values are listed in Table 8. It is obvious that surfaces of TAC-SB samples were the roughest (highest R_a value) due to the harsh abrading conditions. Other parameters such as the mean and maximum roughness depth (R_z and R_{max}, respectively) provided additional information. Table 8 shows that SB samples exhibited deep troughs (up to R_{max} = 24.77 μm ± 19.34 μm and almost R_z = 20 μm in average). These are due to strong impacts of F36 Al_2O_3 particles, projected at 4 bar on the surface of Ti_2AlC. TAC-P80 had different R-values, almost three times lower than TAC-SB. Depressions of less than R_{max} = 1 μm were achieved by polishing Ti_2AlC, the R_a value being close to 100 nm.

SE images showed different oxide morphologies for the three samples after oxidation (Figure 11). The oxide morphology on TAC-OPS samples (Figure 11A) was globular with interconnected fine-grained blisters. They were ~10-20 μm in size. In between, larger faceted grains were evidenced. TAC-P80 (Figure 11B) exhibited unidirectional grooves, in which preferred growth of the large faceted grains was observed. Their size was similar to those observed for TAC-OPS and barely exceeded 10 μm in length for the larger ones. SB specimen (Figure 11C) exhibited similar blister-like structures as for polished samples. They were additionally covered with a substantial fraction of large crystals (~10-20 μm) organized in islands. BSE images (Figure 12), XRD (not shown here) and EDS analyses (not shown here) evidenced α-Al_2O_3 as main oxide, meanwhile larger grains were found to be rutile TiO_2. Analyses (XRD and SEM not shown here) of the SB surface before oxidation showed that the Al_2O_3 content was

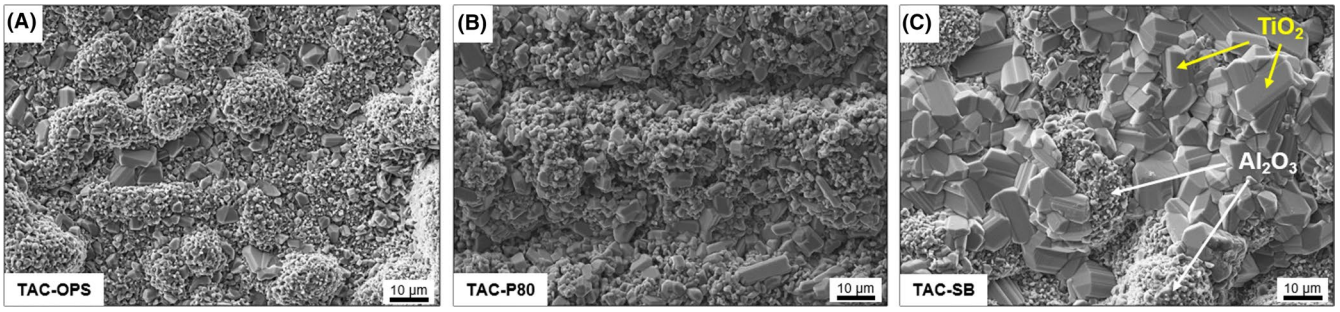

FIGURE 11 SE images of oxidized Ti_2AlC samples with different surface finish: (A) polished to 50 nm colloidal silica, (B) ground with P80 abrasive SiC paper, (C) sandblasted with F36 alumina particles. Oxidation conditions were 1200°C, 50 h in static air [Color figure can be viewed at wileyonlinelibrary.com]

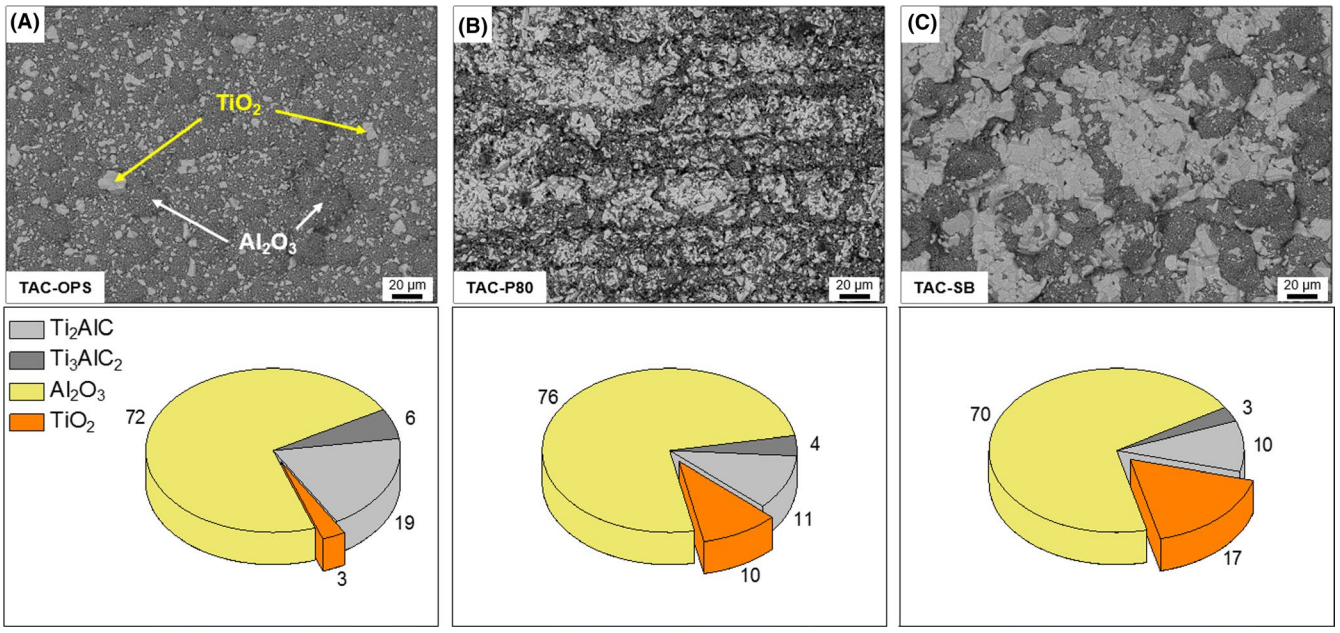

FIGURE 12 BSE images of oxidized Ti_2AlC samples with different surface finish: (A) polished to 50 nm colloidal silica, (B) ground with P80 abrasive SiC paper, (C) sandblasted with F36 alumina particles. Oxidation conditions were 1200°C, 50 h in static air. Corresponding pie charts show results from Rietveld refinement (in wt. %) [Color figure can be viewed at wileyonlinelibrary.com]

non-negligible and evidenced embedding of Al_2O_3 particles in the surface of Ti_2AlC during surface preparation. Rutile's typical elongated prismatic crystal habit with striation along the c-axis[47] was noticed on TAC-SB (Figure 11C) because grains were large enough. TAC-OPS showed small rutile grains (~3-5 μm), scattered across the fine-grained blistered surface of Al_2O_3, and TiO_2 islands of less than 20 μm (Figure 12A). The higher content in MAX phases as compared to TAC-P80 and TAC-SB is on account of less TiO_2 in the analyzed volume. TAC-P80 (Figure 12B) exhibited a significant increase in TiO_2 content and larger light grey patches were observed on BSE images. TiO_2 grain size ranged from submicron to ~15 μm in length, while fine grains of Al_2O_3 composed the remainder of the oxide layer. These results are in agreement with reported features.[3,45,46,48-51] TAC-SB showed a strong increase in TiO_2 content (Figure 12C). In fact, large colonies of TiO_2 crystals, reaching several hundreds of micrometers in size, were observed with BSE images, almost covering the whole surface of the sample. A model was proposed[3] in which rutile TiO_2 grains preferentially grow over depressions initially existing in the base material. The higher roughness is supposed to be the reason of excessive TiO_2 expansion and ensuing grain coarsening.

Cross-sectional analyses (Figure 13) revealed the thickness of Al_2O_3 scale and size of TiO_2 islands. For the three samples, the Al_2O_3 scale was ~8 μm thick, highlighting similar Al-oxidation rates. These results are consistent with reported oxidation outcomes of fine-grained Ti_2AlC.[28] Improved short-term oxidation resistance is indeed expected in such cases due to the fast build-up of the Al_2O_3 scale. In fact, fine-grained microstructures provide multiple pathways through grain boundaries for Al out diffusion, leading to the rapid formation of a thin protective Al_2O_3 layer. In this work, TGA outcomes (not shown here) indicated a rather parabolic oxidation behavior of Ti_2AlC. The coefficient of determination (R^2) for both parabolic and cubic fitting was almost identical, yielding values of 0.999 and 0.990, respectively, but the residual sum of squares indicated a better fit for the parabolic (0.26) than for the cubic behavior (12.08). Despite the fact that fine-grained Ti_2AlC was reported to demonstrate cubic oxidation kinetics[28], in our case, the presence of ~15 wt% Ti_3AlC_2 may have modified the overall oxidation kinetics towards a more parabolic-like behavior, without having a detrimental effect on the oxidation response of the material. Thinner TiO_2 islands/nodules were found atop the Al_2O_3 scale of TAC-OPS (Figure 13A and D) and TAC-P80 (Figure 13B and E) samples. The smooth surface of polished samples (see Table 8) allowed for a smooth Al_2O_3 scale growth (Figure 13D), with few localized spots where delamination occurred. This Al_2O_3 scale appearance is what is most observed in literature, for mirror polished samples.[3,45,46] A more porous and irregular thin Al_2O_3/TiO_2 layer was observed above the dense protective Al_2O_3 scale. The former layer might be the one observed in Figure 11A, there appearing as small protuberances. The Ti_2AlC/Al_2O_3 interface of TAC-P80 showed a more pronounced formation of pores and cracks (Figure 13E). TAC-SB showed a strong undulated profile already before oxidation due to surface preparation (Table 8). Strong rippling/rumpling/ratcheting of the oxide scale was observed (Figure 13C and F). On top of the Al_2O_3 scale, the sections between ripples were filled with large rutile grains as already evidenced on

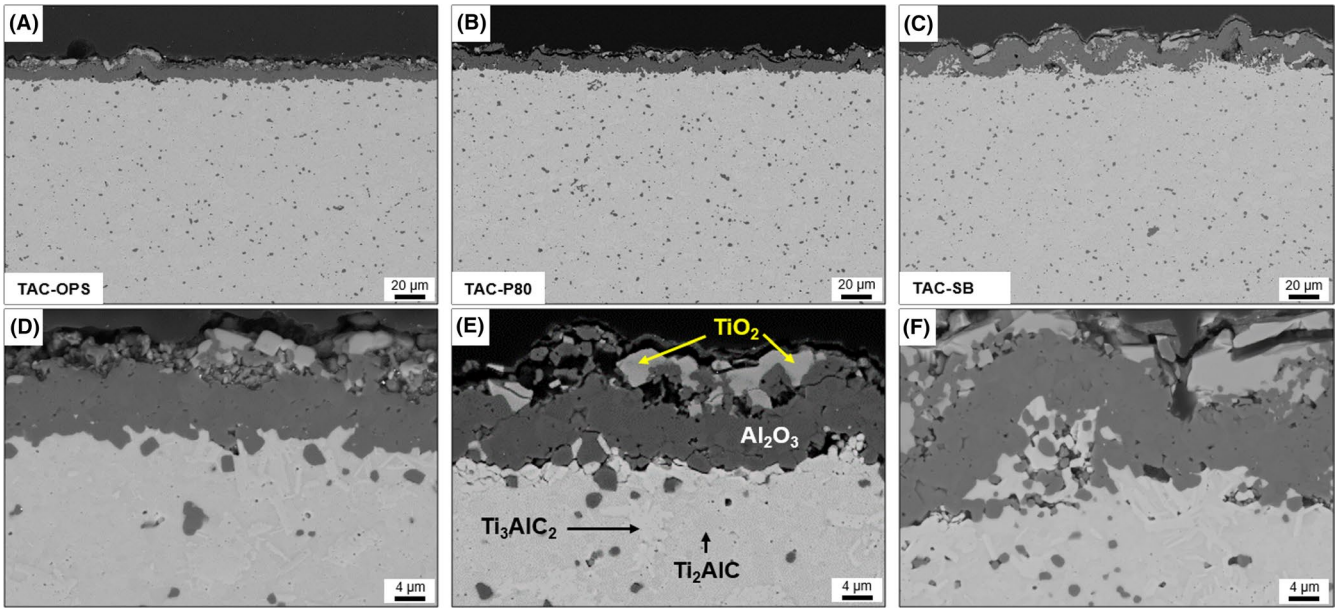

FIGURE 13 Cross-sectional BSE images of oxidized Ti_2AlC samples with different surface finish: (A and D) polished to 50 nm colloidal silica, (B and E) ground with P80 abrasive SiC paper, (C and F) sandblasted with F36 alumina particles. Oxidation conditions were 1200°C, 50 h in static air [Color figure can be viewed at wileyonlinelibrary.com]

previous SEM images (Figures 11C and 12C). Rumpling was observed for MAX phases already, in the case of thermal cycling of SB Cr_2AlC substrates coated with an yttria stabilized zirconia thermal barrier coating.[52] Despite uncertainties as for the cause(s) of rumpling, it was alluded to fast thermal shock conditions, leading to substantial strain during oxide scale growth and thickening. However, in the present case, Ti_2AlC was isothermally oxidized within shorter times (50 hours) as compared to thermal cycling experiments (several hundreds even thousands of hours) and not under cyclic conditions. A common feature though, is the surface roughening procedure employed before oxidation, which in both cases led to initial undulations on the surface of the MAX phase base material and, in all likelihood, to the build-up of internal stresses in the near surface area. The amplitude of these undulations prior to oxidation has a determining role in promoting ratcheting and its critical value, above which rumpling is triggered, tends to decrease with the substrate yield strength.[53] The higher the amplitude, the higher the stresses which initiate rumpling. Additionally, the build-up of in-plane stresses in the Al_2O_3 scale due to lateral growth strain were found by He et al.[53] to arise in the first oxidation cycle and did not substantially change with further cycling. In this work, this would contribute to explain why ratcheting was observed in the case of isothermal oxidation (one-cycle) of Ti_2AlC. In addition, undulation in the oxide scale potentially gave rise to a normal stress component at the Al_2O_3/Ti_2AlC interface, consequently deforming the first layers of the Ti_2AlC base material,[54] which is known to plastically deform at 1200°C.[7] In fact, the equivalent stresses induced in the substrate by the in-plane stresses in the oxide scale were determined to be the largest right underneath recessions in the Al_2O_3 scale.[53] Upon cooling, when the compressive stresses exceed the yield strength of the substrate, the latter plastically deforms allowing the oxide scale to move downwards.

The Al_2O_3 scale is believed to accommodate increasing in-plane compressive stresses by stretching,[54] a phenomenon of release of elastic energy. Thus, the increase in the overall length of the Al_2O_3 scale caused localized buckling and folds, which irremediably led to decohesion between Al_2O_3 and Ti_2AlC as a result of substantial tensile stresses (Figure 13C and F).

Unlike platinum-modified nickel aluminide (PtNiAl) bond coats, for which thermal expansion misfit between Thermally Grown Oxide (TGO) and alloy is well known,[54,55] the mismatch in CTE between Ti_2AlC (8.2×10^{-6}/K between 25°C and 1300°C),[5] Al_2O_3 (8.0×10^{-6}/K and 9.0×10^{-6}/K in the 25°C-1000°C and 25°C-1500°C ranges respectively)[6] and TiO_2 ($8\text{-}9 \times 10^{-6}$/K in the 25°C-1000°C range)[6] is reduced, hence a decrease of the misfit stresses in the Al_2O_3 scale. In addition, for rumpling in EB-PVD TBC systems, typically, the mismatch between substrate and bond coat also plays a significant role. As no bond coat is used here, the given explanations can only be partly applicable. Even though several studies performed on PtNiAl bond coats exist,[54,55] straightforward conclusions about the origin of rumpling and a generalization to other materials (e.g. MAX phases) are still missing.

In this work, we propose a simplified model to simulate the phenomenon of rumpling observed in the case of isothermal oxidation of Ti_2AlC and to highlight a potential correlation with surface roughness prior to oxidation. Growth stresses emerging in the TGO will induce radial stresses at a wavy interface between Ti_2AlC and TGO. TGO growth stresses are assumed to be at a constant level of 1000 MPa in the present model, according to values found in literature,[56] while stress relaxation in the TGO is neglected. The presented model aims to estimate deformation and rumpling of the TGO as a consequence of these stresses. Therefore, the creep deformation of the Ti_2AlC first upper layers as a function of the initial substrate's surface roughness prior to oxidation is calculated. The stress approximation model is based on the stresses in a homogeneous hollow sphere, made of an elastic material, subjected to an internal pressure P. The internal and external radii are denoted a and b respectively (Figure 14A). In the system of spherical coordinates (r, θ, φ), the solution in terms of stress (Figure 14B) for a pure elastic response are as follows[57,58]:

$$\sigma_r = \frac{E}{1-2\nu} \cdot C_1 - \frac{2E}{1+\nu} \cdot C_2 \cdot r^{-3} = -\frac{a^3}{b^3 - a^3} \cdot \left(\frac{b^3}{r^3} - 1\right) \cdot p \qquad \text{(A1)}$$

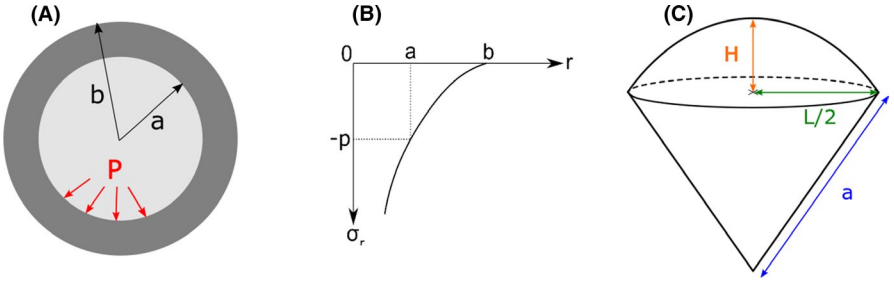

FIGURE 14 Stress approximation model based on stresses in a hollow sphere: (A) cross-section of a homogeneous hollow sphere subjected to internal pressure P, (B) solution in terms of radial stress versus radius of the sphere, (C) section of the sphere considered for the present model [Color figure can be viewed at wileyonlinelibrary.com]

$$\sigma_\theta = \sigma_\varphi = \frac{E}{1-2\nu}\cdot C_1 + \frac{E}{1+\nu}\cdot C_2 \cdot r^{-3} = \frac{a^3}{b^3-a^3}\cdot\left(\frac{b^3}{2r^3}+1\right)\cdot p \tag{A2}$$

$$\sigma_\varphi(a) = \frac{a^3}{b^3-a^3}\cdot\left(\frac{b^3}{2a^3}+1\right)\cdot p = \frac{b^3}{2\left(b^3-a^3\right)}\cdot p + \frac{a^3}{b^3-a^3}\cdot p = \frac{\frac{b^3}{2}+a^3}{\left(b^3-a^3\right)}\cdot p \tag{A3}$$

$$\sigma_\varphi(b) = \frac{a^3}{b^3-a^3}\cdot\left(\frac{1}{2}+1\right)\cdot p = \frac{3}{2}\frac{a^3}{\left(b^3-a^3\right)}\cdot p \tag{A4}$$

$$Atr = a, \sigma_r = p = \frac{b^3-a^3}{\frac{b^3}{2}+a^3}\sigma_\varphi \tag{A5}$$

with E, ν, r, $C1$, and $C2$, respectively, the Young's modulus, the Poisson's ratio, the mean radius of the sphere and constants determined from boundary conditions.

A section of the base material (Ti_2AlC) is considered by taking part of the sphere (Figure 14C), so that one ends up with a cone of slant length a attached to a spherical cap of height H and base radius $L/2$. In the 2D plane, following relations are verified:

$$a^2 = \frac{L^2}{4} + (a-H)^2 \tag{A6}$$

$$\rightarrow 0 = \frac{L^2}{4} - 2aH + H^2; a = \frac{H}{2} + \frac{L^2}{8H} \tag{A7}$$

From expression A6,

$$\rightarrow a - H = \pm\sqrt{a^2 - \frac{L^2}{4}} \tag{A8}$$

$$\rightarrow H = a \pm \sqrt{a^2 - \frac{L^2}{4}} \tag{A9}$$

In this case, only the minus sign gives a meaningful condition. The surface roughness of the material can be approximated by a series of these 3D geometric shapes, the amplitude of surface peaks being directly linked to H. The volume of interest is the volume V of the spherical dome, which is expressed as follows:

$$V = \frac{\pi}{3}H^2(3a-H) = \pi a H^2 - \frac{\pi}{3}H^3 \tag{A10}$$

The time derivative of the volume V divided by the volume is equivalent to the time derivative of deformation ε, which is the creep rate. The creep rate is expressed as follows:

$$\frac{\dot{V}}{V} = \dot{\varepsilon} = \dot{\varepsilon}_0\sigma^n\exp\left(-\frac{U}{RT}\right) \tag{A11}$$

The creep data were retrieved from Barsoum et al.,[59] that is, an activation energy U of 362 kJ/mol, a stress exponent n of 2.5, a minimum creep rate of 1.86×10^{-7} s^{-1} (at 20 MPa, 1000°C). The constant $\dot{\varepsilon}_0$ was calculated using this data and Equation A11, yielding a value of 1.07×10^{-10} s^{-1}. MPa^{-n}. The TGO thickness is given by:

$$d(t_n) = b(t_n) - a(t_n) = k_{ox}\cdot\sqrt{t_n} \tag{A12}$$

During isothermal oxidation at 1200°C, rumpling corresponds to an increase of dome height H, respectively, a decrease of cone slant length a. The determination of the time derivative of a is the next step. According to Equation A9, using the minus sign:

$$\frac{dH}{dt} = \frac{da}{dt} - \frac{2a\frac{da}{dt}}{2\sqrt{a^2-\frac{L^2}{4}}} = \left(1 - \frac{a}{\sqrt{a^2-\frac{L^2}{4}}}\right)\frac{da}{dt} = B(a)\frac{da}{dt} \tag{A13}$$

$$\frac{dV}{dt} = 2H\frac{\pi}{3}\frac{dH}{dt}(3a-H) + \frac{\pi}{3}H^2\left(3\frac{da}{dt} - \frac{dH}{dt}\right) \tag{A14}$$

$$\frac{dV}{dt} = \left\{\frac{2\pi}{3}\left(3aH-H^2\right)B(a) + \pi H^2 - \frac{\pi}{3}H^2B(a)\right\}\frac{da}{dt} \tag{A15}$$

Using A5, A11 and A12:

$$\frac{da}{dt} = \dot{\varepsilon}_0\exp\left(-\frac{U}{RT}\right)\cdot\sigma^n\left(\frac{(a+d(t))^3-a^3}{a^3+\frac{(a+d(t))^3}{2}}\right)^n\cdot\left\{\frac{2\pi}{3}\left(3aH-H^2\right)B(a)+\pi H^2-\frac{\pi}{3}H^2B(a)\right\}^{-1}\cdot V \tag{A16}$$

$$\frac{da}{dt} = \dot{\varepsilon}_0\exp\left(-\frac{U}{RT}\right)\cdot\sigma^n\left(\frac{(a+d(t))^3-a^3}{a^3+\frac{(a+d(t))^3}{2}}\right)^n\cdot\left\{\left(2\pi aH-\pi H^2\right)B(a)+\pi H^2\right\}^{-1}\cdot V \tag{A17}$$

The evolution of a with time increments is calculated by a linear approximation:

$$a(t_{n+1}) = a(t_n) + \frac{da(t_n)}{dt}\cdot(t_{n+1}-t_n) \tag{A18}$$

The evolution of H is then calculated using Equation A9 and with the values of $\frac{da}{dt}$ using Equation A17.

As rumpling appeared to be triggered by increasing surface roughness, the case of sandblasted samples is considered using the model above. H is retrieved from roughness

measurements (see Table 8) and L can be estimated by considering SEM cross-sections of Ti_2AlC right after surface preparation and before oxidation: $H = 3.26$ µm and $L = 100$ µm. According to Equation A7, a is then 13 µm. The TGO thickness is approximately 8 µm after 50 hours at 1200°C (Figure 13F).

The extent to which rumpling occurs is then given by the following relation:

$$X = \frac{H(t_{50}) - H(t_0)}{H(t_0)} \cdot 100\% \tag{A19}$$

with t_0 and t_{50} being the start and the end of the isothermal (T = 1200°C) plateau, respectively.

By plotting the degree of rumpling vs Ti_2AlC surface roughness prior to oxidation (Figure 15A), a steep increase is observed. Smooth surfaces ($R_a < 1$ µm) experience indeed almost no rumpling (max. 0.49%) while rumpling can exceed 600% for surfaces presenting a roughness higher than 6.45 µm. As sandblasted surfaces exhibit higher R values than polished (Figure 15B) and ground surfaces (Table 8), rumpling is essentially observed in these conditions (Figure 15C). The limit to which the system accommodates the deformation is dictated by the interfacial adhesion between TGO and Ti_2AlC and localized decohesion occurs at spots where stress concentration reaches a maximum.

This model shows that rough surfaces (typically achieved with sandblasting) present higher propensity to rumpling. As mentioned earlier, the phenomenon of rumpling is believed to be caused synergistically by different mechanisms and needs further investigation for Ti_2AlC and in general, for MAX phases used in oxidizing environments. The present model thus paves the way for more exhaustive considerations in order to potentially prevent rumpling in systems subjected to similar conditions.

Studies on Ti_3AlC_2 mentioned about the preferential formation of TiO_2 in porous areas[60,61] because of the nature of Al_2O_3 crystal growth. In fact, it was found that low packing of Al_2O_3 crystals in larger cavities facilitate the outward grain boundary diffusion of Ti ions leading to the formation of TiO_2 atop Al_2O_3. Here, similar features may account for the excessive formation of TiO_2 on TAC-SB. More TiO_2 was found above the Al_2O_3 layer as it appears that more from the Ti_2AlC base material was oxidized. At the base material/oxide scale interface, no Ti-rich layer was observed, contrary to what is reported in literature.[28] Instead, the presence of Ti_3AlC_2 clusters was noticed, the same way these clusters were present in the bulk. However, they were always present in the vicinity of TiO_2 colonies.

The oxidation outcomes in the present work can complement the model proposed by Yang et al.,[3] which only considered localized cavities in case of a mirror polished surface. Their theory can be corroborated by taking into account several recesses in the base material and, herewith, a schematic is proposed (Figure 16). With cavities less than 2 µm in size, they found that the thickness of rutile was almost zero. No large TiO_2 colonies were indeed observed in the present work for polished surfaces with a roughness below 1 µm. Some rutile grains were disseminated over the Al_2O_3 scale, without forming a consistent layer. Valleys are filled with Al_2O_3 first since Al atom self-diffusion along (0001) basal planes in Ti_2AlC requires low activation energy.[62] Al is not entirely depleted in the surface's vicinity. Al_2O_3 within cavities are found to be present in small equiaxed grains on account of curved surfaces and subsequent multiple nucleation on existing grains.[3] When larger depressions are present, additional Al diffuses out, gradually leading to exhaustion of the A-element content in near-surface areas. For cavity sizes ranging from 2 to 6 µm, Yang et al.[3] observed ~3-5 µm thick rutile crystals. In the present work, an increase in rutile content was also observed for ground surfaces with similar roughness (see R_z in Table 8), with preferential growth within recesses (grooves in the non-oxidized state). The depletion in Al is even more pronounced with increasing surface roughness because its diffusion from peaks towards valleys is multidirectional. The same occurred with Ti, hence more TiO_2 was found filling valleys above Al_2O_3 in TAC-SB. Diffusion pathways for Ti across the equiaxed microstructure are numerous and eased due to loose packing of Al_2O_3 crystals. For cavities larger than 6 µm, the thickness of TiO_2 almost doubled.[3]

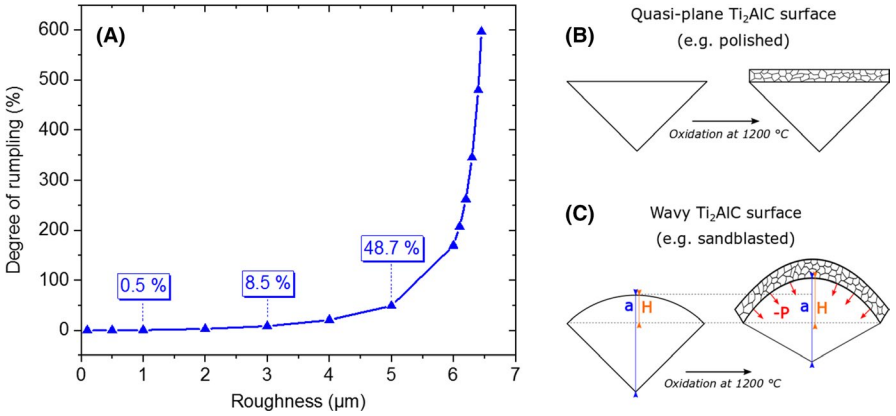

FIGURE 15 TGO rumpling during isothermal oxidation of Ti_2AlC: (A) Evolution of TGO rumpling with increasing Ti_2AlC surface roughness prior to oxidation, (B) quasi-plane surfaces (typically polished or gently ground) do not experience rumpling while (C) rough surfaces (typically sandblasted) show significant rumpling [Color figure can be viewed at wileyonlinelibrary.com]

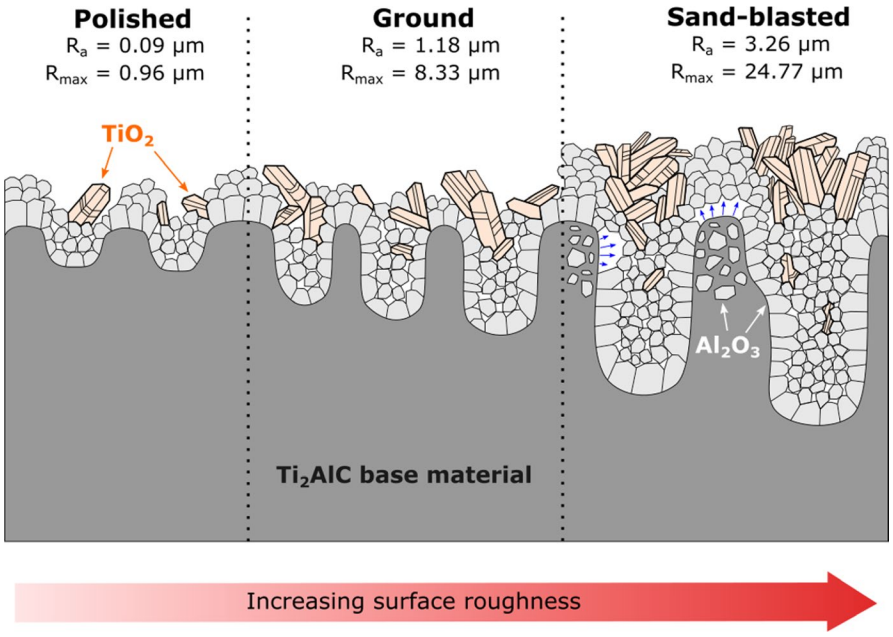

FIGURE 16 Schematic of surface roughness/oxidation response relationship for Ti_2AlC. Blue arrows indicate decohesion of the Al_2O_3 scale [Color figure can be viewed at wileyonlinelibrary.com]

Additionally, the growth rate of TiO_2 is much higher than that of Al_2O_3.[3] Therefore, a great amount of large rutile grains was observed in SB samples in the present work. Some of them formed up to ~10 µm thick layers within valleys of ripples above the Al_2O_3 scale.

A trend was observed in which increasing roughness leads to the formation of larger amounts of TiO_2 above the protective Al_2O_3 scale. The thickness of the latter is invariant with increasing roughness, though, due to large undulations on the substrate's surface before oxidation, the total length of Al_2O_3 after oxidation of sandblasted samples was the largest, hence more Al was depleted in that case. Above a critical amplitude of undulations present before oxidation, the oxide scale started to rumple, followed by localized failure of the Ti_2AlC/Al_2O_3 interface. The microstructure and impurity concentration being identical in all instances, one can say that the observed differences in oxide morphology are exclusively correlated to a surface roughness dependent mechanism.

4 | CONCLUSIONS

Ti_2AlC powder was synthesized by the means of the newly invented molten salt shielded synthesis (MS^3) route. The molten potassium bromide salt improved atomic inter-diffusion of elemental constituents. The optimal synthesis parameters were as follows: a temperature of 1000°C, lower than for conventional routes, a Ti:Al:C = 2:1:0.9 molar ratio, and a holding time of 5 hours. Ti_2AlC powders with an optimal purity of 91 wt. % were rapidly produced and the MAX phase yield was 97 wt. % (Ti_2AlC and Ti_3AlC_2). The powder agglomerates exhibited a globular morphology and were composed of a multitude of submicron sized primary particles.

Pressureless sintering at 1300°C in argon resulted in incomplete densification and increasing the sintering temperature to 1400°C promoted the phase conversion of Ti_2AlC to Ti_3AlC_2 and a reduction in Ti_2AlC purity. Therefore, FAST/SPS was required to almost fully densify Ti_2AlC, achieving a relative density of 98.5% at 1200°C and 50 MPa. Dense Ti_2AlC samples did not show texture and their microstructure was fine-grained with an average grain size below 1 µm, indicating that this sintering method had no influence on grain growth.

The fine-grained microstructure was an advantage during oxidation experiments. Multiple pathways for Al out-diffusion allowed for fast buildup of protective Al_2O_3 scales atop Ti_2AlC specimen. Surface roughness strongly influenced the morphology of the oxide scale. Smooth surfaces were mainly composed of small Al_2O_3 grains with preferential growth of rutile observed above recesses initially present in the base material. Rough surfaces showed more disproportionate formation of rutile crystals. It is assumed that protrusions were areas where rapid Al depletion occurred, followed by outward diffusion of Ti through Al_2O_3 grain boundaries. Large rutile islands were found above Al_2O_3 scales in sandblasted samples. A phenomenon of scale rumpling (or ratcheting) was noticed for latter samples, most probably due to a synergy between various mechanisms. It is believed that strong roughening of the Ti_2AlC surface by sandblasting coupled with growth stresses in the thermally grown Al_2O_3 scale promoted its rumpling, causing interfacial decohesion.

These outcomes complement data about oxidation of Ti_2AlC gathered in the last decades and are worth being considered in the case of high-temperature applications in oxidative media.

ACKNOWLEDGMENTS

This work has been funded by the Germany's Federal Ministry of Education and Research ("Bundesministerium für Bildung und Forschung") under the MAXCOM project (03SF0534). The authors thank Dr Doris Sebold (IEK-1), Beatrix Göths (IEK-4) for SEM/EDS and Dr Egbert Wessel (IEK-2) for EBSD measurements. Open access funding enabled and organized by Projekt DEAL.

ORCID

Sylvain Badie https://orcid.org/0000-0001-9988-8465
Apurv Dash https://orcid.org/0000-0002-4869-3104
Yoo Jung Sohn https://orcid.org/0000-0002-7994-7269
Robert Vaßen https://orcid.org/0000-0002-9198-3991
Olivier Guillon https://orcid.org/0000-0003-4831-5725
Jesus Gonzalez-Julian https://orcid.org/0000-0002-4217-8419

REFERENCES

1. Barsoum MW. The $M_{n+1}AX_n$ phases: a new class of solids. Prog Solid State Chem. 2000;28:201–81.
2. Barsoum MW, El-Raghy T. Synthesis and characterization of a remarkable ceramic: Ti_3SiC_2. J Am Ceram Soc. 1996;79:1953–6.
3. Yang HJ, Pei YT, Rao JC, De Hosson JTM, Li SB, Song GM. High temperature healing of Ti_2AlC: on the origin of inhomogeneous oxide scale. Scr Mater. 2011;65:135–8.
4. Li S, Song G, Kwakernaak K, van der Zwaag S, Sloof WG. Multiple crack healing of a Ti_2AlC ceramic. J Eur Ceram Soc. 2012;32:1813–20.
5. Barsoum MW, El-Raghy T, Ali M. Processing and characterization of Ti_2AlC, Ti_2AlN, and $Ti_2AlC_{0.5}N_{0.5}$. Metall Mater Trans A. 2000;31:1857–65.
6. Morrell R. Handbook of properties of technical & engineering ceramics Pt.1, an introduction for the engineer and designer. Richmond: H.M. Stationery Office. 1985;348 p.
7. Barsoum MW, Brodkin D, El-Raghy T. Layered machinable ceramics for high temperature applications. Scr Mater. 1997;36:535–41.
8. Kisi EH, Wu E, Zobec JS, Forrester JS, Riley DP. Inter-conversion of $M_{n+1}AX_n$ phases in the Ti-Al-C system. J Am Ceram Soc. 2007;90:1912–6.
9. Wang X, Zhou Y. Solid-liquid reaction synthesis and simultaneous densification of polycrystalline Ti_2AlC. Zeitschrift für Met. 2002;93:66–71.
10. Gauthier-Brunet V, Cabioc'h T, Chartier P, Jaouen M, Dubois S. Reaction synthesis of layered ternary Ti_2AlC ceramic. J Eur Ceram Soc. 2009;29:187–94.
11. Benitez R, Kan WH, Gao H, O'Neal M, Proust G, Radovic M. Room temperature stress-strain hysteresis in Ti_2AlC revisited. Acta Mater. 2016;105:294–305.
12. Zhou AG, Barsoum MW. Kinking nonlinear elastic deformation of Ti_3AlC_2, Ti_2AlC, $Ti_3Al(C_{0.5}, {}_{N0.}5)2$ and $T_i2Al(_{C0.}5, {}_{N0.}5)$. J Alloys Compd. 2010;498:62–70.
13. Kulkarni SR, Wu AVDK-H. Synthesis of Ti_2AlC by spark plasma sintering of TiAl–carbon nanotube powder mixture. J Alloys Compd. 2010;490:155–9.
14. Sleptsov SV, Bondar AA, Witusiewicz VT, Hecht U, Hallstedt B, Petyukh VM, et al. Cocrystallization of MAX-Phases in the Ti–Al–C system. Powder Metall Met Ceram. 2015;54:471–81.
15. Yeh CL, Shen YG. Effects of TiC and Al_4C_3 addition on combustion synthesis of Ti_2AlC. J Alloys Compd. 2009;470:424–8.
16. Hendaoui A, Vrel D, Amara A, Langlois P, Andasmas M, Guerioune M. Synthesis of high-purity polycrystalline MAX phases in Ti–Al–C system through mechanically activated self-propagating high-temperature synthesis. J Eur Ceram Soc. 2010;30:1049–57.
17. Rutkowski P, Huebner J, Kata D, Chlubny L, Lis J, Witulska K. Thermal properties and laser processing of hot-pressed materials from Ti–Al–C system. J Therm Anal Calorim. 2019;137:1891–902.
18. Khoptiar Y, Gotman I. Ti_2AlC ternary carbide synthesized by thermal explosion. Mater Lett. 2002;57:72–6.
19. Galvin T, Hyatt NC, Rainforth WM, Reaney IM, Shepherd D. Molten salt synthesis of MAX phases in the Ti-Al-C system. J Eur Ceram Soc. 2018;38:4585–9.
20. Spencer CB, Córdoba JM, Obando N, Sakulich A, Radovic M, Odén M, et al. Phase evaluation in Al_2O_3 fiber-reinforced Ti_2AlC during sintering in the 1300°C-1500°C temperature range. Zhou Y, editor. J Am Ceram Soc. 2011;94:3327–34.
21. Pang WK, Low IM, O'Connor BH, Peterson VK, Studer AJ, Palmquist JP. In situ diffraction study of thermal decomposition in Maxthal Ti_2AlC. J Alloys Compd. 2011;509:172–6.
22. Zhang Z, Lim SH, Lai DMY, Tan SY, Koh XQ, Chai J, et al. Probing the oxidation behavior of Ti_2AlC MAX phase powders between 200 and 1000°C. J Eur Ceram Soc. 2017;37:43–51.
23. Dash A, Vaßen R, Guillon O, Gonzalez-Julian J. Molten salt shielded synthesis of oxidation prone materials in air. Nat Mater. 2019;18:465–70.
24. Dash A, Sohn YJ, Vaßen R, Guillon O, Gonzalez-Julian J. Synthesis of Ti_3SiC_2 MAX phase powder by a molten salt shielded synthesis (MS^3) method in air. J Eur Ceram Soc. 2019;39:3651–9.
25. Tallman DJ, Anasori B, Barsoum MW. A critical review of the oxidation of Ti_2AlC, Ti_3AlC_2 and Cr_2AlC in air. Mater Res Lett. 2013;1:115–25.
26. Barsoum MW. Oxidation of $Ti_{n+1}AlX_n$ (n=1-3 and X=C, N): I. Model. J Electrochem Soc. 2001;148:C544.
27. Barsoum MW, Tzenov N, Procopio A, El-Raghy T, Ali M. Oxidation of $Ti_{n+1}AlX_n$ (n=1-3 and X=C, N): II. Experimental results. J Electrochem Soc. 2001;148:C551.
28. Yu W, Vallet M, Levraut B, Gauthier-Brunet V, Dubois S. Oxidation mechanisms in bulk Ti_2AlC: influence of the grain size. J Eur Ceram Soc. 2020;40:1820–8.
29. Basu S, Obando N, Gowdy A, Karaman I, Radovic M. Long-term oxidation of Ti_2AlC in air and water vapor at 1000–1300°C temperature range. J Electrochem Soc. 2011;159:C90–C96.
30. Smialek JL. Unusual oxidative limitations for Al-MAX phases. NASA/TM—2017-219444. 2017;1–29 p.
31. Zolotoyabko E. Determination of the degree of preferred orientation within the March-Dollase approach. J Appl Crystallogr. 2009;42:513–8.
32. Wang C-A, Zhou A, Qi L, Huang Y. Quantitative phase analysis in the Ti–Al–C ternary system by X-ray diffraction. Powder Diffr. 2005;20:218–23.
33. Bai Y, He X, Li Y, Zhu C, Zhang S. Rapid synthesis of bulk Ti_2AlC by self-propagating high temperature combustion

synthesis with a pseudo–hot isostatic pressing process. J Mater Res. 2009;24:2528–35.
34. Fan Q, Chai H, Jin Z. Microstructural evolution in the combustion synthesis of titanium carbide. J Mater Sci. 1996;31:2573–7.
35. Sujata M, Bhargava S, Sangal S. On the formation of $TiAl_3$ during reaction between solid Ti and liquid Al. J Mater Sci Lett. 1997;16:1175–8.
36. Školáková A, Leitner J, Salvetr P, Novák P, Deduytsche D, Kopeček J, et al. Kinetic and thermodynamic description of intermediary phases formation in Ti-Al system during reactive sintering. Mater Chem Phys. 2019;230:122–30.
37. Liu X, Zhang S. Low-temperature preparation of titanium carbide coatings on graphite flakes from molten salts. J Am Ceram Soc. 2008;91:667–70.
38. Shatynski SR. The thermochemistry of transition metal carbides. Oxid Met. 1979;13:105–18.
39. Chen Y, Chu M, Wang L, Bao X, Lin Y, Shen J. First-principles study on the structural, phonon, and thermodynamic properties of the ternary carbides in Ti-Al-C system. Phys status solidi. 2011;208:1879–84.
40. Chen CC. Phase equilibria at Ti–Al interface under low oxygen pressure. Atlas J Mater Sci. 2014;1:1–11.
41. Zhou WB, Mei BC, Zhu JQ, Hong XL. Rapid synthesis of Ti_2AlC by spark plasma sintering technique. Mater Lett. 2005;59:131–4.
42. Tzenov NV, Barsoum MW. Synthesis and characterization of Ti_3AlC_2. J Am Ceram Soc. 2004;83:825–32.
43. Hashimoto S, Takeuchi M, Inoue K, Honda S, Awaji H, Fukuda K, et al. Pressureless sintering and mechanical properties of titanium aluminum carbide. Mater Lett. 2008;62:1480–3.
44. Gonzalez-Julian J, Classen L, Bram M, Vaßen R, Guillon O. Near net shaping of monolithic and composite MAX phases by injection molding. Travitzky N, editor. J Am Ceram Soc. 2016;99:3210–3.
45. Smialek JL. Oxidation of Al_2O_3 scale-forming MAX phases in turbine environments. Metall Mater Trans A. 2018;49:782–92.
46. Song GM, Schnabel V, Kwakernaak C, van der Zwaag S, Schneider JM, Sloof WG. High temperature oxidation behaviour of Ti_2AlC ceramic at 1200°C. Mater High Temp. 2012;29:205–9.
47. Li W-J, Shi E-W, Yin Z-W. Growth habit of rutile and α-Al_2O_3 crystals. J Cryst Growth. 2000;208:546–54.
48. Wang XH, Zhou YC. High-temperature oxidation behavior of Ti_2AlC in air. Oxid Met. 2003;59:303–20.
49. Byeon JW, Liu J, Hopkins M, Fischer W, Garimella N, Park KB, et al. Microstructure and residual stress of alumina scale formed on Ti_2AlC at high temperature in air. Oxid Met. 2007;68:97–111.
50. Sonestedt M, Frodelius J, Sundberg M, Hultman L, Stiller K. Oxidation of Ti_2AlC bulk and spray deposited coatings. Corros Sci. 2010;52:3955–61.
51. Cui B, Jayaseelan DD, Lee WE. Microstructural evolution during high-temperature oxidation of Ti_2AlC ceramics. Acta Mater. 2011;59:4116–25.
52. Gonzalez-Julian J, Go T, Mack DE, Vaßen R. Thermal cycling testing of TBCs on Cr_2AlC MAX phase substrates. Surf Coatings Technol. 2018;340:17–24.
53. He MY, Evans AG, Hutchinson JW. The ratcheting of compressed thermally grown thin films on ductile substrates. Acta Mater. 2000;48:2593–601.
54. Balint D, Hutchinson J. An analytical model of rumpling in thermal barrier coatings. J Mech Phys Solids. 2005;53:949–73.
55. Tolpygo VK, Clarke DR. On the rumpling mechanism in nickel-aluminide coatings. Acta Mater. 2004;52:5115–27.
56. Lima CRC, Dosta S, Guilemany JM, Clarke DR. The application of photoluminescence piezospectroscopy for residual stresses measurement in thermally sprayed TBCs. Surf Coatings Technol. 2017;318:147–56.
57. Maddux GE, Vorst LA, Giessler JF, Moritz T. Stress analysis manual. Air Force Flight Dyn Lab. 1969.
58. Timoshenko S. Part II: Advanced theory and problems. In: Strength of materials (p. 510). 2nd ed. D. New York, NY: Van Nostrand Company; 1940.
59. Tallman DJ, Naguib M, Anasori B, Barsoum MW. Tensile creep of Ti_2AlC in air in the temperature range 1000–1150°C. Scr Mater. 2012;66:805–8.
60. Drouelle E, Gauthier-Brunet V, Cormier J, Villechaise P, Sallot P, Naimi F, et al. Microstructure-oxidation resistance relationship in Ti_3AlC_2 MAX phase. J Alloys Compd. 2020;826:154062.
61. Song GM, Pei YT, Sloof WG, Li SB, De Hosson JTM, van der Zwaag S. Oxidation-induced crack healing in Ti_3AlC_2 ceramics. Scr Mater. 2008;58:13–6.
62. Wang J, Zhou Y, Liao T, Zhang J, Lin Z. A first-principles investigation of the phase stability of Ti_2AlC with Al vacancies. Scr Mater. 2008;58:227–30.

How to cite this article: Badie S, Dash A, Jung Sohn Y, Vaßen R, Guillon O, Gonzalez-Julian J. Synthesis, sintering, and effect of surface roughness on oxidation of submicron Ti_2AlC ceramics. *J Am Ceram Soc*. 2021;104:1669–1688. https://doi.org/10.1111/jace.17582